3D detection of flying insects from a millimeter-wave radar imaging system

Etienne Dedic, Dominique Henry, Mathieu Lihoreau, Hervé Aubert

3D Detection of Flying Insects from a Millimeter-Wave Radar Imaging System

Authors – Etienne Dedic [ab], Dominique Henry [a], Mathieu Lihoreau [bc], Hervé Aubert [ab]

[a] LAAS, CNRS, 31400, Toulouse, France, {ededic, dhenry, haubert}@laas.fr

[b] Toulouse University, Toulouse, France

[c] CRCA-CBI, CNRS, 34000 Toulouse, France, mathieu.lihoreau@univ-tlse3.fr

Corresponding author: ededic@laas.fr

Abstract – Studying the movement patterns of small flying insects, such as pollinators, is a major challenge in biology. Here we introduce an original approach to track the 3D motion of flying insects using a millimeter-wave radar imaging system. 3D images are obtained from the beam scanning of a Frequency-Modulated Continuous-Wave and Single-Input Multiple-Output radar operating at 77 GHz. We derive the flight trajectory of insects and mitigate the electromagnetic clutter from the 3D radar images. To illustrate our approach, 3D flights of isolated bumblebees are radar tracked in a limited volume during 5.2 minutes with a time resolution of 60ms. The radar tracks are compared with video recordings for validation purpose. The tracking volume of an insect using a single radar is estimated at 5.3m^3, and we show that the volume can be tripled when three radar imaging systems are deployed. Finally, we discuss how our new radar-based technique can be extended to track a broad diversity of small flying animals at different spatial scales and simultaneously in the lab and in the field.

Keywords – Animal tracking, Millimeter-wave, Radar imaging

1 Introduction

How flying insects, such as bees, wasps, flies and butterflies, move across landscapes to exploit plant or host resources is a central question in biology, with far reaching applications for pollination, food production, pest management and conservation. However, direct observations of the foraging patterns of these small insects in naturalistic conditions have always been difficult (Freeman, 1968). For instance, tracking a flying bee requires to monitor a small target (typically less than 2cm long) with high velocity (up to 20km/h), moving in the 3D space, and sometimes over several square kilometers over many days (Chittka, 2022). This is out of reach with current tracking technologies despite recent technical advances (Kays et al., 2015).

In the last decades, many remote sensing technologies (optical, radio but also by other means) have been explored to study insect behaviour (Drake and Reynolds, 2013; Kissling et al., 2014; Reynolds and Riley, 2002). Emerging technologies for entomology have been reviewed recently in (Rhodes et al., 2022; van Klink et al., 2022). Many of these technologies aim at recording the movement patterns of pollinators while foraging on flowers. High Frequency (HF) Radio Frequency IDentification (RFID) sensors (Kim et al., 2019; Ohashi et al., 2010), computer vision (Crall et al., 2018; Manoukis and Collier, 2019), and motion detection cameras (Crall et al., 2015; Lihoreau et al., 2016a) have been used to record nest entrance and flower visits by individual bees. These techniques can be applied to monitor the foraging activity of bees and estimate their flower visitation sequences over long periods of time (up to weeks). However they provide no information about the flight trajectories and search patterns of bees between flower visits. At small spatial scales, flight paths can be recorded with optical approaches. For instance a single Infra-Red (IR) camera has been used to track bumblebees and moths equipped with photoluminescent tags outdoor within about 2.0m^2 (Walter et al., 2021). A so-called Fast-Lock-On (FLO) tracking system based on a single stereo camera and an IR illumination source (Vo-Doan et al., 2023) enabled for high-resolution video recording of a lightly-tagged flying insect motion during natural behavior. High-speed cameras have also been used to study the 3D movements of untagged bees in

the lab (Ings and Chittka, 2008; Lihoreau et al., 2016b) and outdoor within about 27m^3 (Sun and Gaydecki, 2021), but these approaches are highly sensitive to illumination and typically require several cameras to resolve 3D tracks.

The aforementioned techniques enable observations of complete behavioural sequences in small laboratory setups where naturalistic behaviour may be expressed only to a limited extent, or partial flight paths in the field. Radio-Frequency (RF) technologies, such as harmonic radar (Riley et al., 1996; Woodgate et al., 2017), radio-telemetry (Kennedy et al., 2018), Vertical-Looking Radar (VLR) (Drake and Reynolds, 2013) provide means to study the spatial movements of flying insect over larger spatial scales in the field. An extensive review of these RF-based entomology techniques can be found in (Drake and Reynolds, 2013; Kissling et al., 2014). Scanning harmonic radar and radio-telemetry enable to detect insects in 2D (range-azimuth) at up to several hundred meters but at the cost of poor spatial resolution (down to ten meters), poor temporal resolution (down to a second), and large power consumption (up to tens of kW) (Kissling et al., 2014; Psychoudakis et al., 2008). These long-range tracking approaches also require to equip the insects with large tags whose mass and size may impact the insect's flight: typically about 12 mg and 16 mm long in the case of harmonic radar (Drake and Reynolds, 2013; Kissling et al., 2014; Psychoudakis et al., 2008); typically 300 mg and a footprint of 100mm^3 for radio-telemetry (Kim et al., 2019). Harmonic radar allows only detection of one transponder at a time, whereas radio-telemetry allows detection of multiple tags simultaneously. However, harmonic transponders are very light-weight compared to the active tags used in radio-telemetry and thus allows them to be used on a wider range of insects. The effect of the tag weight on the insect behaviour has been studied for terrestrial and flying insects in e.g. (Batsleer et al., 2020; Kaláb et al., 2021) and recently reviewed for the case of beetles in (Růžičková and Elek, 2023). These techniques, initially implemented with a stationary transmitter, have recently been integrated on Unmanned Aerial Vehicles (UAVs) (Ju and Son, 2022; Kim et al., 2022; Lavrenko et al., 2021; Tahir and Brooker, 2015) to improve the tracking distance and reduce power consumption. Similarly, the optical sensor used in (Walter et al., 2021) was

estimated to be sufficiently light-weight to be mounted on a UAV, thus opening the possibility to track flying insects over larger spatial volumes. Moreover, the so-called FLO tracking system developed in (Vo-Doan et al., 2023) has been integrated on a UAV to track a tagged insect. Recently, a high-resolution camera mounted on a static UAV hovering over a field allowed to track butterflies in an area of about 2,000 m^2 (Margerie and Monmasson, 2024). Although promising results were obtained, tracking flying insects using UAV-integrated tracking radio-systems has not been demonstrated yet.

Here we introduce a millimeter-wave radar imaging system to track the 3D motion of flying insects with a high spatio-temporal resolution, and at various spatial scales. In contrast with optical-based techniques that require multiple cameras to resolve the insect position in 3D (Lihoreau et al., 2016b), a single radar sensor can be used. Radars are not affected by the brightness and thus outside observations are possible irrespective of light conditions (even at night-time). Radars can be tuned in order to control resolution and detection range to the targets. Finally, millimeter waves can penetrate the opaque thin nets or thin plexiglas walls, enabling to track insects in cluttered environments. In a preliminary study (Dore et al., 2020), we demonstrated that bumblebees can be detected up to 2.0 meters (±0.05 meters) using such a mm-wave radar. The detection range increases with the transmitted power and the size of the target (in most cases) and thus the use of a low-power mm-wave radar sensor and the small size of the target only enable detection at small distances. The detection range for such small targets is very small compared to that obtained from other aforementioned techniques such as harmonic radar and RF telemetry. However a recent study (Dore et al., 2020) showed that a mm-wave radar allowed to track in 3D with high-resolution which is interesting from an ethological point-of-view even at small spatial scales (Ings and Chittka, 2008; Lihoreau et al., 2016b). In this previous study (Dore et al., 2020), the basic algorithm used to mitigate the electromagnetic clutter drastically limited the number and duration (<2 seconds) of motion tracking. In this new study, we establish, for the first time, the proof-of-concept of a new detection algorithm to detect a flying insect over longer periods (several minutes) using a home-made millimeter-wave imaging system. To do so we tagged bumblebees with a

small hollow aluminum cylinder (1.5 cm long, 1.0 mm in diameter and 100 µm of thickness and 50 mg of mass) and released them alone in a flight chamber for 37 minutes. We then applied an original detection algorithm based on the mitigation of the electromagnetic clutter from isolines in the 3D radar images. Using a categorical classification technique, we compared the 3D tracks of flying bumblebees derived from the radar system with those obtained by using video recordings.

2 Materials and methods

2.1 Millimeter-wave radar imaging system

2.1.1 Definition of the transmitted and received radar signals

The block diagram of the radar imaging system is shown in Figure 1a. The system includes a Frequency-Modulated (FM) Continuous-Wave (CW) Single-Input Multiple-Output (SIMO) radar commercialized by INRAS GmbH (INRAS, 2023). The radar transmits periodically the waveform displayed in Figure 2. During each period or repetition time t_{rep}, the frequency-modulated signal, i.e. the sweep, with ramp duration t_{ramp} (=205µs), carrier frequency f_c (=77GHz) and modulation bandwidth B (=3GHz) is transmitted by N_{T_X}(=1) transmitting antenna. The electromagnetic power P_{T_X} radiated by the radar is of 10dBm. The transmitted signal is then backscattered by the scene, received by N_{R_X}(=16) antennas of the radar and processed by a Field-Programmable Gate Array (FPGA) that is connected to a computer via an Ethernet link. Transmitting (T_X) and receiving (R_X) antennas are identical vertically-polarized rectangular patch antenna arrays, printed on the same circuit board. At every moment nt_{rep}, where n=0, 1,…, N_L-1, the sweep is generated by the transceiver of the radar front-end and radiated by the T_X-antenna. The N_L time samples 0, t_{rep}, $2t_{rep}$, $3t_{rep}$, …, $(N_L-1)t_{rep}$ are usually called the slow time samples. Let N_S be the number of so-called fast time samples used to digitize the waveform of Figure 2. The maximum detection range, denoted R_{max}, of the sensor is given by $\frac{N_S \Delta R}{2}$, where N_S denotes the number of fast time samples and ΔR is the theoretical range resolution of the radar, that is, $\Delta R = c/2B$ where c denotes the speed of light in vacuum (ΔR=5cm for B=3GHz).

2.1.2 3D scanning of the radar beam

Since the off-the-shelf FMCW SIMO radar steers electronically the beam only in a plane, for 3D tracking purpose we perform a mechanical beam scanning in elevation using a rotating reflector to sweep the beam in elevation. As illustrated in Figure 1b, the reflector is a metallic plate placed in front of the radar antennas and rotates at angular frequency ω_α (rad/s). The dimensions of the rectangular plate must be such that most of the radar beam radiated by the T_X antenna is intercepted by the reflector, when its surface faces the antenna or equivalently, when the unit vector $\vec{n}$ normal to the reflector surface is also normal to the radiating surface of the radar (α=0° or 180° in Figure 1b). To meet this requirement, the rectangular plate of 20cm×25cm is placed at the distance z_0 of 15cm in front of the radar antennas.

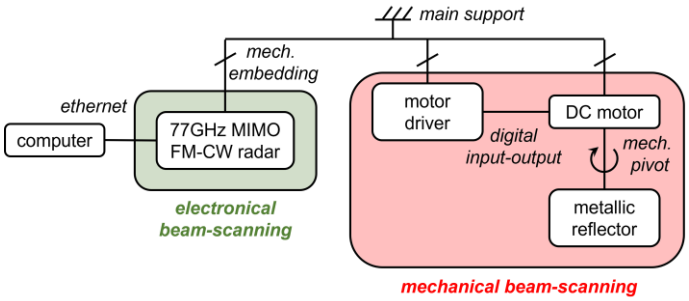

(a)

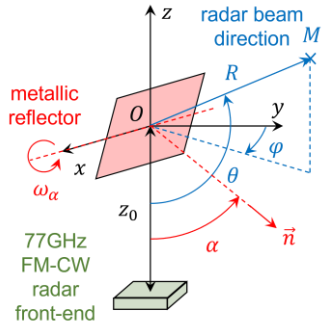

(b)

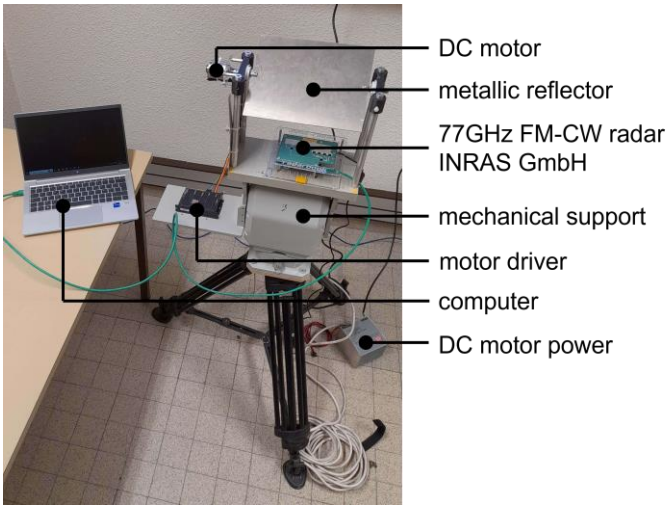

(c)

Figure 1 – Millimeter-wave radar imaging system: (a) Block diagram of the system used to steer mechanically the radar beam in elevation and electronically in azimuth; (b) Definition of the azimuth angle φ and elevation angle θ of the radar beam direction, and of the angle α between the unit vector -$\vec{z}$ of the *z*-axis and unit vector $\vec{n}$ normal to the reflector surface; (c) Photo of the millimeter-wave radar imaging system used to track the motion of flying insects.

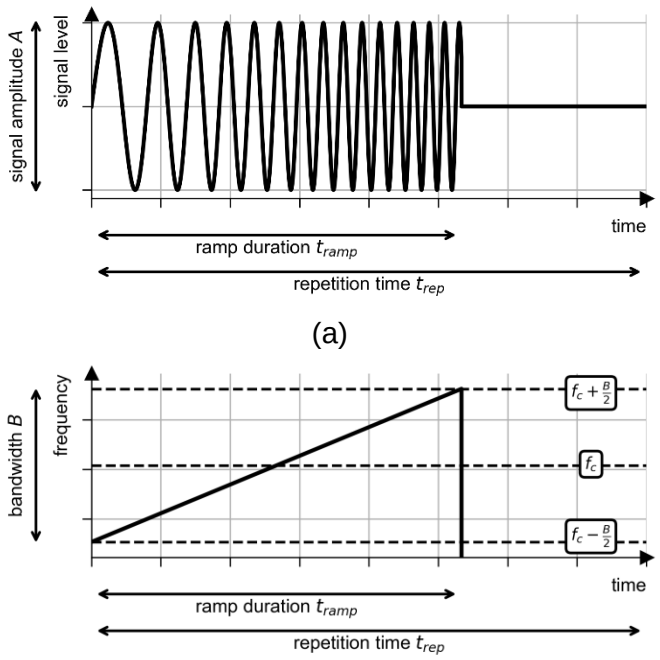

Figure 2 – Frequency modulated waveform periodically transmitted by the T_X-antenna of the radar: (a) level and (b) frequency of the waveform as a function of time. f_c and B denote respectively the operating frequency and modulation bandwidth of the transmitted FM signal, called the *sweep*, while t_{rep} designates the period or repetition time, and t_{ramp} is the ramp duration of the (linear) modulation of the sweep. During each period, the signal is transmitted only during the duration t_{ramp} of the ramp.

Let θ and φ denote respectively the elevation and azimuth angles of the radar beam direction (see Figure 1b). According to the laws of reflection, the elevation angle θ of the radar beam direction is twice the angle α between the unit vector $-\vec{z}$ of the z-axis and unit vector $\vec{n}$ normal to the reflector surface. During one full rotation of the reflector, α ranges from 0° to 360° and therefore, each point in the 3D scene is illuminated twice by the radar beam. As sweeps are sequentially transmitted at times 0, t_{rep}, $2t_{rep}$, $3t_{rep}$, …,$(N_L\text{-}1)t_{rep}$ by the T_X-antenna, the step angle $\Delta\theta$ of beam elevation between two successive sweep transmissions is given by $2\omega_\alpha t_{rep}$. To prevent blind spots in elevation, the step $\Delta\theta$ must be smaller than the half-power beamwidth (13.2°) of the radar T_X-antenna. To meet this requirement, we set t_{rep}=1ms and ω_α=500rpm, which leads to $\Delta\theta$=6°. Therefore, during 1 second, the radar beam scans the 3D scene 16.7 times. However, the DC motor used in our experiment to drive the

rotation of the reflector does not provide a constant angular rotation speed. Indeed, the standard deviation (over 1024 samples) of the angular frequency is of 45rpm and as a result, during radar measurement the scan rate in elevation ranges from 16 scans/s to 17.5 scans/s. Therefore, the use of the time average for the scan rate to determine the elevation angle of the radar beam direction can result in a large inaccuracy in estimating the 3D location of the targets. To avoid such inaccuracy, the scan rate is estimated over time by deriving the elevation angle of the reflector from the beat frequency spectrum obtained at the radar-to-reflector distance. Such spectrum is displayed in Figure 3a, in which higher peaks of echo level occur periodically at the distance z_0 (±2cm) from the radar radiating surface, that is, when the unit vector $\vec{n}$ normal to the reflector surface is also normal to the radiating surface of the radar (α=0° or 180°). As angular speed is assumed to be constant between two successive peaks, the variation of elevation angle over time can be derived from the time intervals between two peaks and from the knowledge of the rotation direction –clockwise or counterclockwise– of the reflector (see Figure 3b). As explained above, the proposed mechanical beamscanning system allows to estimate the range and angle of arrival of a target but does not allow to estimate the speed of a target from a Doppler analysis of the raw radar data. Indeed, estimating the speed from a Doppler analysis requires recording samples along the slow time axis for the same elevation angle which is not achievable using the proposed solution as the elevation angle changes along slow time. From our approach, we estimated the target location in 3D space and computed the instantaneous speed from the location samples through time.

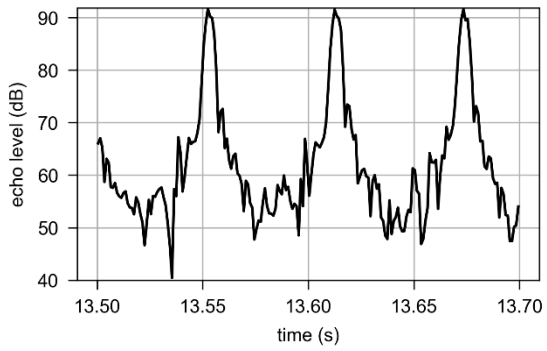

(a)

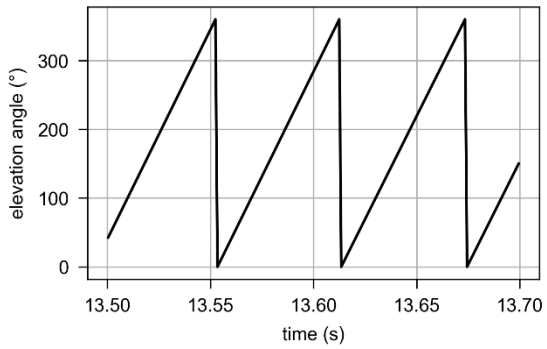

(b)

Figure 3 – (a) Beat frequency spectrum at the radar-to-reflector distance z_0=15cm during the rotation of the reflector (higher peaks occur when α=0 and 180°); (b) estimated elevation angle of the radar beam as a function of time derived from the time intervals between two successive peaks in the beat frequency spectrum and for a clockwise direction of the reflector rotation (angular speed is assumed to be constant between two successive peaks).

2.1.3 Generation of 3D images from the millimeter-wave radar scanning system

From the raw data collected by the R_X-antennas of the radar system, 3D images are generated from the following step-by-step process illustrated in Figure 4:

i. At each slow time sample nt_{rep} where n=0, 1,…, N_L-1, one chirp is transmitted by the N_{T_X}(=1) T_X-antenna and backscattered by the scene. The signals received by the N_{R_X}(=16) R_X-antennas of the radar are then digitized and stored in a matrix called the *frame* F_n of dimensions $N_C \times N_S$, where $N_C=N_{T_X}N_{R_X}$. From such raw data collection obtained at slow time nt_{rep}, each row of the frame is multiplied by the appropriate calibration complex-valued vector provided by the radar manufacturer (INRAS, 2023). Frames $F_0, F_2,\ldots F_{N_L-1}$ obtained respectively at slow time samples $0,t_{rep},\ldots,(N_L-1)t_{rep}$ are finally stacked in a matrix of dimensions $N_L \times N_C \times N_S$ (see Figure 4a);

ii. At each slow time sample nt_{rep} where n=0, 1,…, N_L-1, the elevation angle θ_n of the radar beam direction is estimated from the beat frequency spectrum, as described in section 2.1.2.

The matrix M of dimensions $N_L \times N_C \times N_S$ is then built, as illustrated in Figure 4b;

iii. Two sampling grids are next built:

(1) the *range sampling grid* $R=[R_0,R_1,\ldots,R_{N_S-1}]$ where N_S is the number of samples used to digitize the range R and $R_i=i\Delta R$, with i=0,…,N_S-1, and

(2) the *azimuth sampling grid* $\Phi=[\varphi_0,\varphi_1,\ldots,\varphi_{N_C-1}]$. To point the radar beam in the azimuth angle φ_k, with k=0,…,N_C-1, the phase shift $\Delta\phi_k (= 2\pi k/N_C - \pi)$ between two adjacent receiving antennas must be equal to $2\pi\frac{d}{\lambda}\sin(\varphi_k)$, where d is the distance between the antennas and λ is the free-space wavelength at the operating frequency f_c. Therefore, the azimuth angle φ_k in the sampling grid Φ is given by $\arcsin\left(-\frac{\lambda}{2d}+k\frac{1}{N_C}\frac{\lambda}{d}\right)$. To avoid spatial aliasing, this angle must range between -90° and +90° and therefore, the distance d between two antennas must not exceed half-wavelength. As $d=\lambda/2$ (=1.95mm) for the radar used here in our system, the azimuth angle φ_k equals $\arcsin\left(-1+k\frac{2}{N_C}\right)$, with k=0,…,$N_C$-1;

iv. 2D MUSIC (MUltiple SIgnal Classification) algorithm reported in (Manokhin et al., 2015) is applied separately to each frame F_n (n=1, 2,…, N_L) of the matrix M. This discrete source DOA estimation algorithm estimates the so-called *2D-MUSIC score function* for the range and azimuth angles. Each pixel (i,k) in the corresponding 2D-space image of dimension $N_C \times N_S$ contains a *MUSIC score* $P_n[i,k]$ at the range-azimuth (R_i,φ_k). The zero-padding is next applied by using the padding factors p_R and p_φ for the range and azimuth axes, respectively. Therefore, the padded number $N_{FFT,R}$ for the range samples is given by $2^{\lceil \log_2 N_S \rceil + p_R}$, while the padded number $N_{FFT,\varphi}$ for the azimuth samples is given by $2^{\lceil \log_2 N_C \rceil + p_\varphi}$, where $\lceil\cdot\rceil$ denotes the ceiling function. The number N_φ of samples required to build the MUSIC score function for the azimuth angle is then of $N_{FFT,\varphi}$. To avoid spatial aliasing,

negative frequencies of the frequency spectrum for the range are discarded and therefore, the number N_R of samples required to build the MUSIC score function for the range is only of $N_{FFT,R}/2$. Finally, the range and azimuth angle in uniformly padded sampling grids are then respectively given by $R_i=i\frac{N_S}{N_R}\Delta R$ and $\varphi_k=\arcsin\left(-1+k\frac{2}{N_\varphi}\right)$, where i=0,…,$N_R$-1 and k=0,…,$N_\varphi$-1. In addition, each voxel (i,k,n) in the 3D-space matrix of dimension $N_R \times N_\varphi \times N_L$ contains the value of the MUSIC score $P_n[i,k]$ at the spherical coordinates (R_i, φ_k, θ_n), where n=0, 1,…, N_L-1 (see Figure 4c). The size N_{tot} of data recorded during $\Delta t=(N_L-1)t_{rep}$ is then given by $N_R N_\varphi N_L n_0$, where n_0 is the number of bits used to code each echo level in the pixelized 2D-space image.

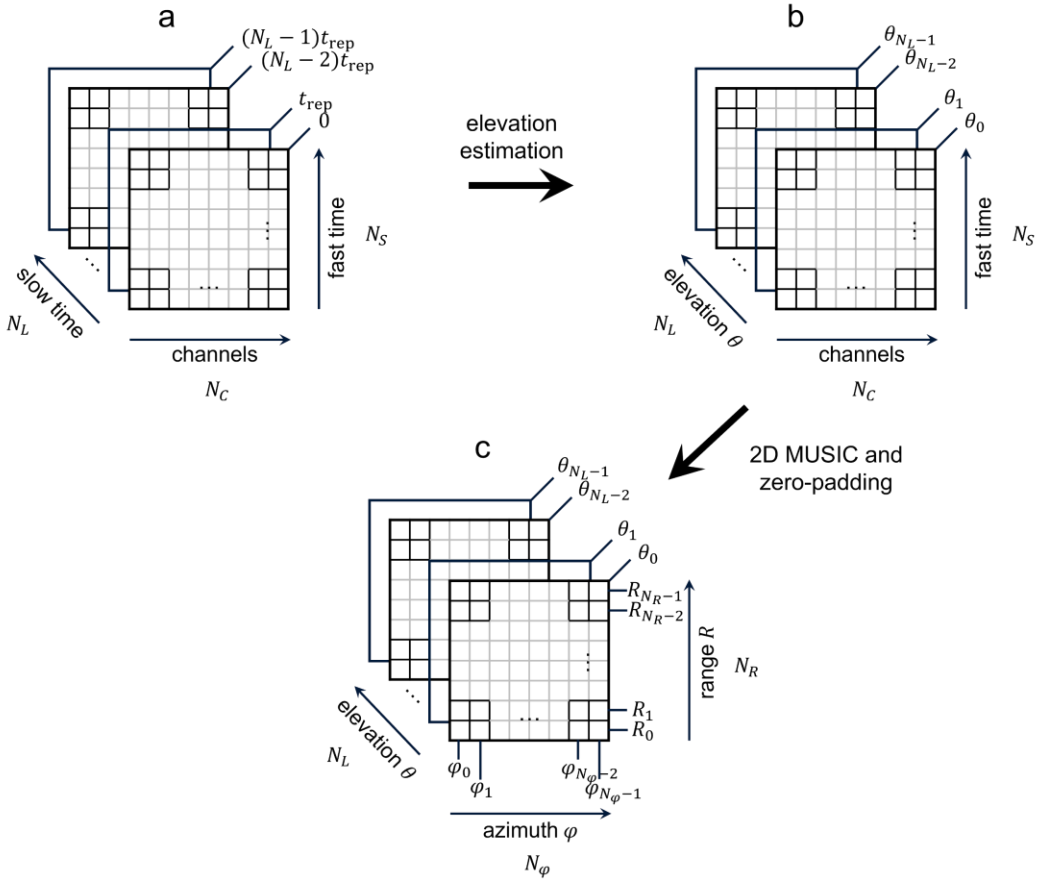

Figure 4 – Illustration of the generation of the 3D-space radar images from the millimeter-wave radar scanning system: (a) radar data are sorted by increasing slow time; (b) radar data are sorted by increasing elevation angle; (c) 3D-space radar matrix.

2.1.4 Electromagnetic clutter mitigation, detection and tracking algorithms

A well-known and widely-used detection algorithm in radar image processing is the Constant False Alarm Rate (CFAR) algorithm (Finn and Johnson, 1968). Variations of this algorithm were applied recently for automotive detection using the Area-Based CFAR (Wei et al., 2023), and by us to monitor the sow postural activity from the so-called Cell-Averaging CFAR (Henry et al., 2023).

Here, a novel detection algorithm is proposed to detect and locate flying insects in a 3D environment from radar images. This detection algorithm enables both to mitigate the electromagnetic clutter (i.e., the undesirable radar echoes radar echoes from electromagnetic backscattering of the environment) and to estimate flight path of insects. Let us detail each step of the algorithm illustrated in Figure 5a:

i. Following section 2.1.3, the 3D-space matrix of dimensions $N_R \times N_\varphi \times N_L$ is generated from the beam scanning of the environment in absence of flying insects (see Figure 6a). Each voxel (i,k,n) in the matrix contains the value of the MUSIC score $P_n^{ref}[i,k]$ at the spherical coordinates (R_i, φ_k, θ_n), where $R_i = i\frac{N_S}{N_R}\Delta R$, $\varphi_k = \arcsin\left(-1+k\frac{2}{N_C}\right)$ and θ_n is the elevation angle of the radar beam direction derived from step *ii* in section 2.1.3 and $\theta_n - 2\pi\left\lfloor\frac{\theta_n}{2\pi}\right\rfloor$ is the associated principal angle. Let B_m be the set of 2D-space images obtained at elevation angles ranging from $(m-1)\Delta\theta$ to $m\Delta\theta$, with m=0, 1,…, N_θ-1, where $N_\theta = 2\pi/\Delta\theta$, and let $\bar{\theta}_m$ be the arithmetic mean of this set (see Figure 6b). Then, we build the image $\bar{P}_m^{ref}$ in which the pixel (i,k) contains the arithmetic mean of MUSIC scores at the pixel (i,k) of all images in the set B_m (see Figure 6c). From the stacking of the reference 2D-space images $\bar{P}_0^{ref}$, $\bar{P}_1^{ref}$, …, $\bar{P}_{N_\theta-1}^{ref}$, the so-called *reference 3D-space image* of dimensions $N_R \times N_\varphi \times N_L$ is finally derived;

ii. The segmentation algorithm illustrated in Figure 5b is applied to the images $\bar{P}_m^{ref}$ (with m=0, 1,…, N_θ-1) of the reference 3D-space image derived at step *i*, that is, in the absence of flying insects. Each $N_R \times N_\varphi$ image (Figure 7a) is segmented by using *isolines* (Figure 7b): along an isoline, the

radar echo keeps a constant level (Henry and Aubert, 2019). The calculation of isolines is adaptive (input parameters of the algorithm are dependent on features of the image to be segmented). An isoline borders a surface on which the level and position of the highest MUSIC score is determined (see Figure 7c): if this level is higher than a predefined threshold P_{min} (e.g., P_{min}=-47dB), we assert that this MUSIC score contributes significantly to the electromagnetic clutter. Following this criterion, the *reference clutter* contributors are selected in the images $\overline{P}_1^{ref}$, $\overline{P}_2^{ref}$, …, $\overline{P}_{N_\theta-1}^{ref}$ and characterized by their respective azimuth-range locations and MUSIC scores for N_θ elevation angles;

iii. In the presence of insects, the so-called *target 3D-space matrix* is generated from the beam scanning of the scene during the measurement time Δt. We apply the segmentation algorithm based on isolines on each $N_R \times N_\varphi$ image derived from the target 3D-space matrix. At this step of the process, local maxima of MUSIC scores that are higher than the predefined threshold P_{min} originate either from the insects to be detected or from the electromagnetic clutter. They form a set of *unclassified* contributors, that are characterized by their respective range-azimuth-elevation coordinates and MUSIC scores. Range-azimuth-elevation coordinates of unclassified contributors are finally mapped into Cartesian coordinates;

To decide if an unclassified contributor originates from an insect or from the electromagnetic clutter, we calculate the distances between this contributor and those detected in the reference image at step *ii*. If at least one distance is below the pre-defined d_{min} threshold, then we assert that the contributor is brought by the electromagnetic clutter, otherwise it originates from the insect (Figure 8c). Following this criterion, position of the insect is determined over time (Figure 8d). The threshold distance d_{min} can be derived from the reference 3D-space image in absence of insects. For this purpose, the aforementioned segmentation based on isolines is applied on each 2D-space image i with i=0,…,N_L-1 of the reference recording and provides a set of $N_{iso,i}$ isolines. Then, the barycenter of each isoline is computed and stored. We obtain a set of

barycenter $B_{k,i}$ where k=0,…,$N_{iso,i}$-1 and i=0,…,N_L-1. The shortest Euclidean distance from the set of distances $|B_{k,i}-B_{l,j}|$ for $(l,j)\in[0,\ldots,N_{iso,i}-1]\times[0,\ldots,N_L-1]-(k,i)$ is then determined and stored for each k=0,…,$N_{iso,i}$-1 and i=0,…,N_L-1 thus yielding a set of size $N_{iso,0}+N_{iso,1}+\ldots+N_{iso,N_L-1}$. The longest distance of this set is named the *reference distance* and is denoted by d_{ref} (here, d_{ref}=15cm) [remark : In (Dedic et al., 2023) we proposed a clutter mitigation algorithm in which the classification is carried out by calculating the distances between each point of the isoline while here, only the distance between the level of highest echo within the isoline and contributor is computed. This results in a significant reduction in the computation time];

iv. A simple spatial smoothing method is devised to build the target tracks from the set of target detections. Each detection $\left(R_{target,k}, \varphi_{target,k}, \theta_{target,k}\right)$ of the set of target detections is labeled with a timestamp $t_{target,k}$ at the elevation angle $\theta_{target,k}$ such that $t_{target,k}=\left\lfloor\frac{\theta_{target,k}}{2\pi}\right\rfloor\frac{1}{f_{scan}}$, where f_{scan} (=16.7 scans/s) is the scan rate. Thus, detections for which the elevation angle is closer than 2π may have the same associated timestamp. Then the set of target detections is sorted by increasing timestamps. We assume that only one target is present in the scanned scene so we assume no ambiguous track assignments to resolve. For each timestamp, we compute the barycenter of the sub-sets of detections for which the timestamp is identical so as to obtain only one detection per timestamp. The so-called *target track* is then the obtained set of barycenters sorted by increasing timestamp.

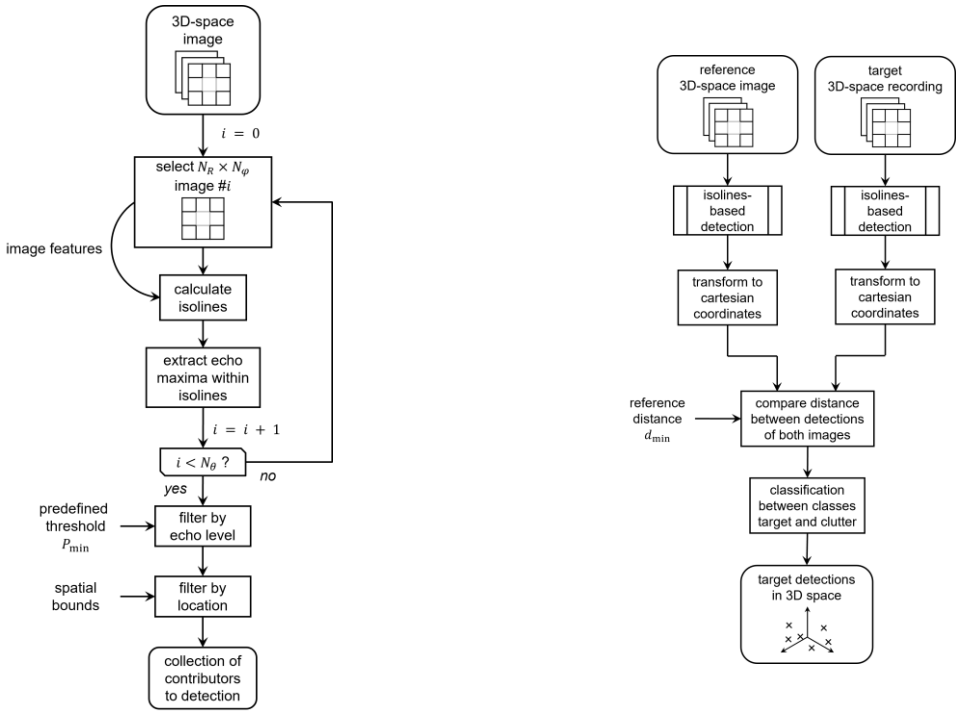

(a) (b)

Figure 5 – Block diagrams of the detection algorithm applied on a 3D-space image: (a) clutter mitigation process, (b) isolines-based detection subroutine to extract maxima from a 3D-space image using segmentation by isolines.

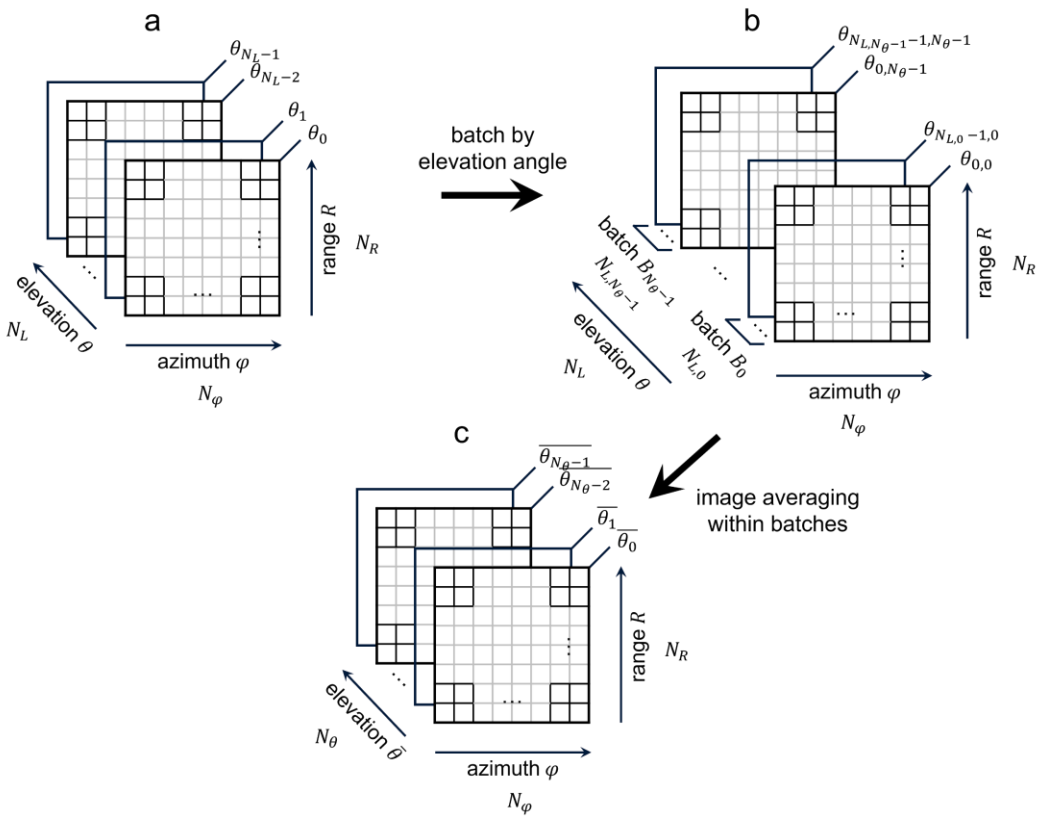

290

291 **Figure 6 – Derivation of the reference 3D-space image from the 3D-space recording matrix of the environment in**
292 **absence of flying insects: (a) Reference 3D-space radar recording matrix, (b) reference 3D-space radar recording**
293 **matrix sorted by increasing batch rank of elevation angles and (c) reference 3D-space image.**

294

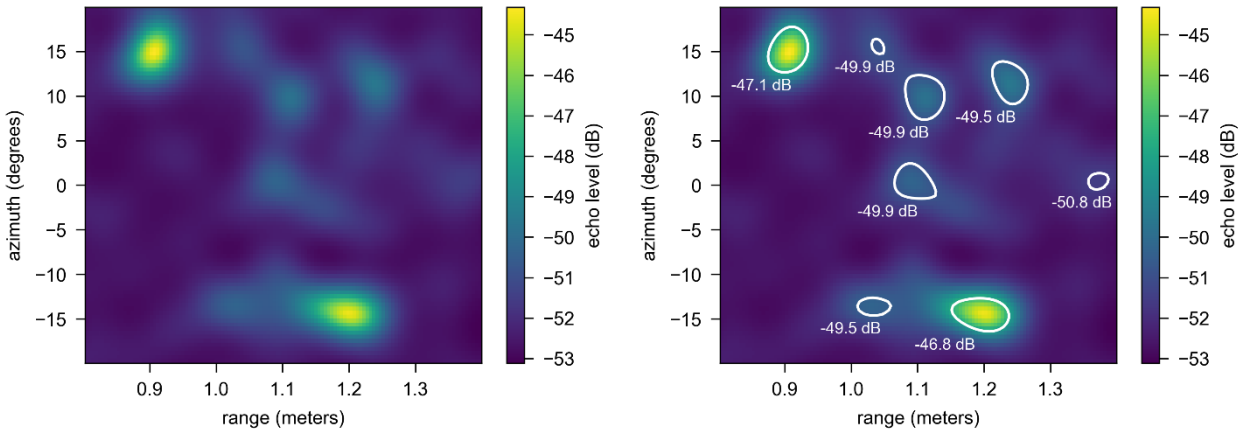

(a) (b)

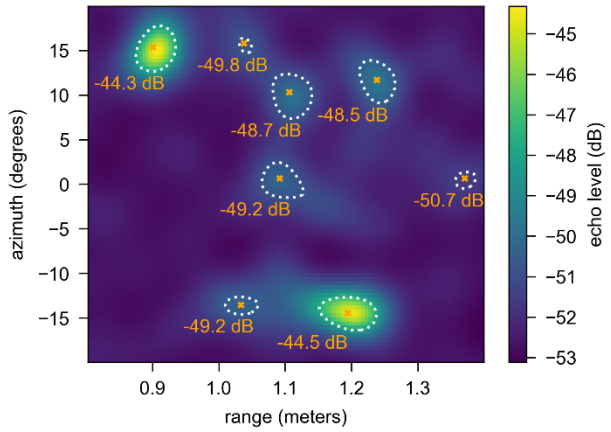

(c)

Figure 7 – Illustration of the calculation of isolines applied to a 2D image: (a) range-azimuth mapping of MUSIC scores (namely the *MUSIC score function*), (b) calculated isolines (solid, white) with associated isoline levels (white) superimposed on the MUSIC score function, (c) derived detection points (solid, orange) with associated detection MUSIC score (in dB) (solid, orange) and isolines (dotted, white) superimposed on the MUSIC score function.

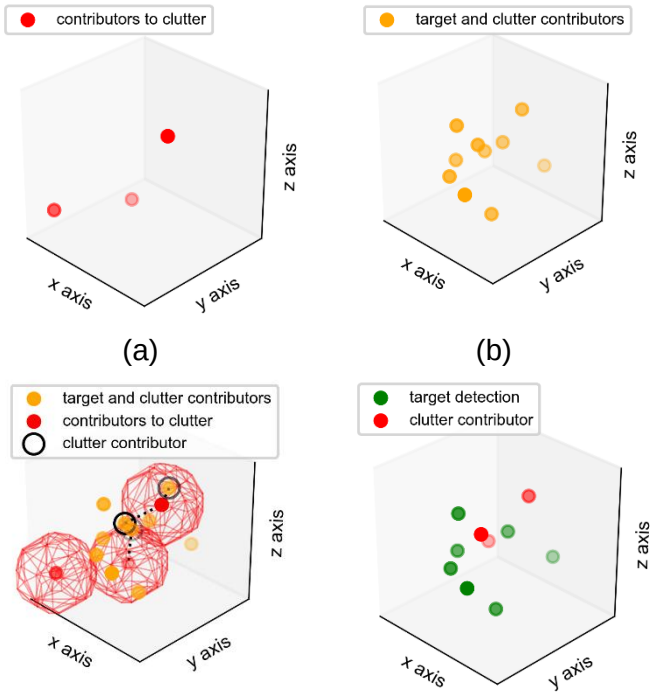

(a) (b)

(c) (d)

Figure 8 – Illustration of the process to mitigate the electromagnetic clutter: (a) location (in red) of contributors to the clutter in the reference image; (b) locations (in orange) of unclassified contributors that originate either from an insect or from the electromagnetic clutter; (c) location of contributors to clutter of Figure 8a (in red) of unclassified contributors of Figure 8b (in orange) and of contributors selected as originating from the electromagnetic clutter (in black, solid). The contributors to the clutter are such that their distance to the closest reference clutter contributor (in black, dotted) is included in the volume of the red meshed polygon shown in Figure 8(c); (d) estimated location of the insect (in green) and of the contributors to electromagnetic clutter (in red).

2.2 3D motion tracking of bumblebees

2.2.1 Experimental setup

The proposed radar detection system and algorithm were applied to track bumblebees (*Bombus terrestris*) from commercially obtained hives (Koppert, The Netherlands). The measurements were performed in a 20×10×4 m^3 outside flight tent (Figure 9a) at the experimental apiary of the CRCA-CBI (Toulouse, France). We applied the new detection algorithm based on the clutter mitigation technique described in Section 2.1.4 and we increased the electromagnetic reflectivity of the bumblebees by equipping them with a small hollow aluminum cylinder of 1.5 cm long, 2.0 mm in diameter and 100 µm of thickness. The simulated Radar Cross-Section of the cylinder at the radar working frequency (77GHz) is of -31dBsm. The weight of the cylinder was about 50mg, that is, only 13% of the average weight of a bumblebee (400mg). Preliminary detection results showed that 3D motion of this cylinder inside the two flight cages can be tracked by the radar system (see Supplementary materials, Figure S2). Here we constrained the movements of the bumblebees within the radar detection volume by using flight cages made of materials (thin plastic films foam and polyester) weakly reflecting to millimeter-waves. We used two flight cages with different volumes: in the Setup #1, the cuboid cage of 0.22m^3 was made of cellophane for the cube faces and foam for the edges (see Figure 9a), while in Setup #2 the cage was made of polyester net which delimits the larger volume of 1.5m^3 (see Figure 9b). For comparison purposes, 2D video recordings of the detection volume have been made during the radar scanning by using a single video camera.

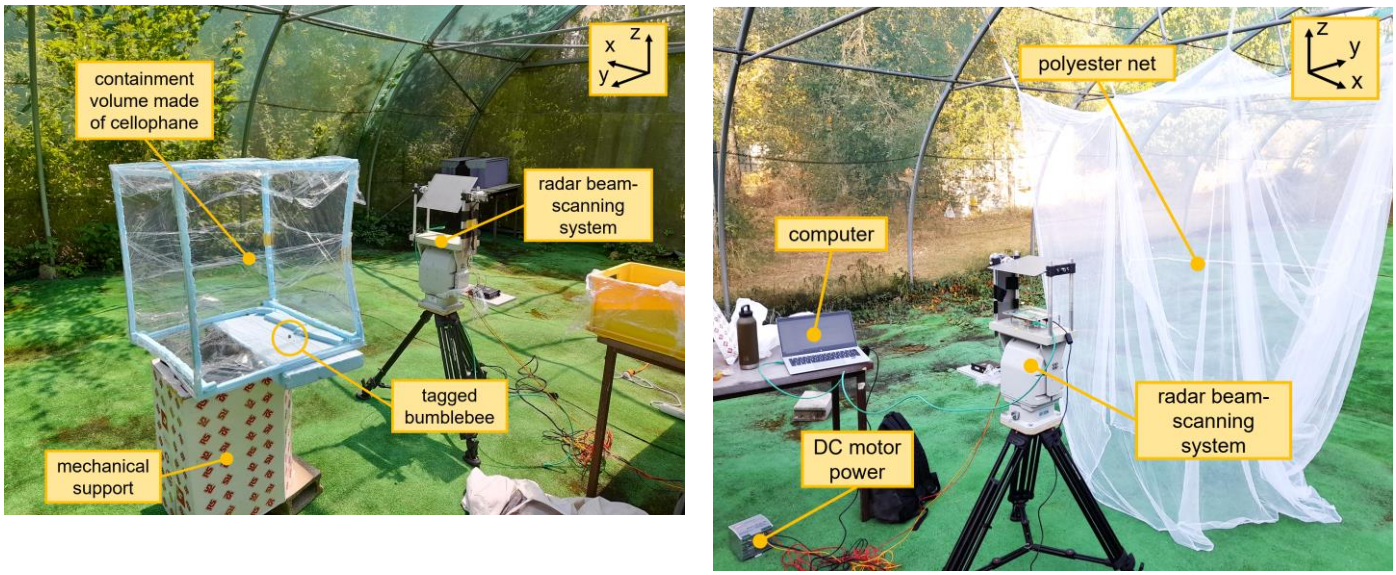

(a) (b)

Figure 9 – Photos of the experimental setup: (a) setup #1; (b) setup #2. The volume that restrained the movements of the insect was placed in front of the radar beam-scanning system. Cartesian (x, y, z) coordinates are specified in insert.

2.2.2 Measurement protocol

The radar tracking system was used for single target tracking, meaning that only one bumbleee was tracked at a time. All tested bumblebees came from the same colony. Before the measurements, bees were cold-anaesthetized at -12°C and equipped with metallic cylinder attached to their thorax using cyanoacrylate gel glue (Loctite SuperGlue 3). We selected rather large individuals in order to reduce the mass ratio between the cylinder and the bee. As described in 2.1.4, the calibration of the experimental setup was performed by scanning the radar beam in the flight cage in absence of insects. A bee was then introduced in Setup #1 or Setup #2. The motion of one bee (bee #1) was tracked in Setup #1 on 2023-06-30, and that of two other bees (bee #2 and bee #3), one after the other, in Setup #2 on 2023-08-23. Radar measurements were carried out for a total observation time of about 37 minutes (362s for bee #1, 1167s for bee #2, 691s for bee #3) under a hot sunny morning for both setups. After the collection of radar data and video recordings, bees returned to their colony nest.

2.2.3 Data analysis

Five features (see Table 1) were annotated manually for all video recordings and considered as ground-truth (see Supplementary materials Figure S1). At each given recorded moment, the location of the bee

in Cartesian coordinates (x_v,y_v,z_v) was annotated relatively to the origin placed at the center of the rotating axis of the beam scanning system. Therefore, a bee located at the bottom left front corner of the confinement volume would be assigned the location (x_v=0,y_v=0,z_v=0). A bee located close to computed reference clutter contributors would be assigned c_v=1. The bee's activity m_v was also annotated. For instance, a bee flying in the confinement volume would be assigned the activity m_v=1. For each video, we identified the 3D position of the bee relative to the radar system, the proximity of the bee to highly cluttered areas, and the activity of the bee. All the recorded features were binary features and Pearson correlation matrices were computed. Automated analyses (described in Section 2.1.4) were used to extract 3D tracks from the radar data. Instantaneous speed was numerically estimated from the 3D tracks. To compare bee tracks from video recordings with those from radar recordings, binary classifications were applied on the positional features and instantaneous speed extracted from radar recordings. Confusion matrices were then evaluated for each feature and conclusions were drawn on the accuracy of the radar tracking system. Statistical analyses were performed using Python 3.9.0 with statistical packages NumPy 1.23.5, SciPy 1.9.3, SciKit-Learn 1.3.0. Graphical representations were rendered using MatPlotLib 3.6.3.

Table 1 - Description of the features annotated from the manual analysis of the video recordings. The reference clutter contributors are extracted from the reference 3D-space image.

feature name	type	definition	feature values	
			0	1
x_v	binary categorical	Cartesian position of the bee relatively to the radar system	left	right
y_v			close	far
z_v			low	high
m_v		bee's activity	moving slow	moving fast
c_v		proximity to reference clutter contributors	far	close

3 Results

3.1 Video analyses

Annotated features statistics are shown in Figure 10. In setup #1, bee #1 was in cluttered areas (mostly corners of the confinement box) during 277s out of the 362s (76%) whereas in setup #2, bees #2 and

#3 were in cluttered areas only during 120s out of the 2,336s (5.1%). This is because less electromagnetic clutter contributors per unit of volume was generated in setup #2 compared with setup #1. Moreover, from Figure 10b, the high correlation between the features m_v (activity of bees) and c_v (proximity to highly cluttered areas) (coefficient of determination: R^2=0.53) reflects the fact that bee #1 was often not moving while being in cluttered areas of the scene (mostly corners). From Figure 10a, the bees spent most of their time (>60%) in the upper part (z_v=1) of the confinement volume in both experimental setups and were mostly moving slowly (m_v=0) inside the confinement volume.

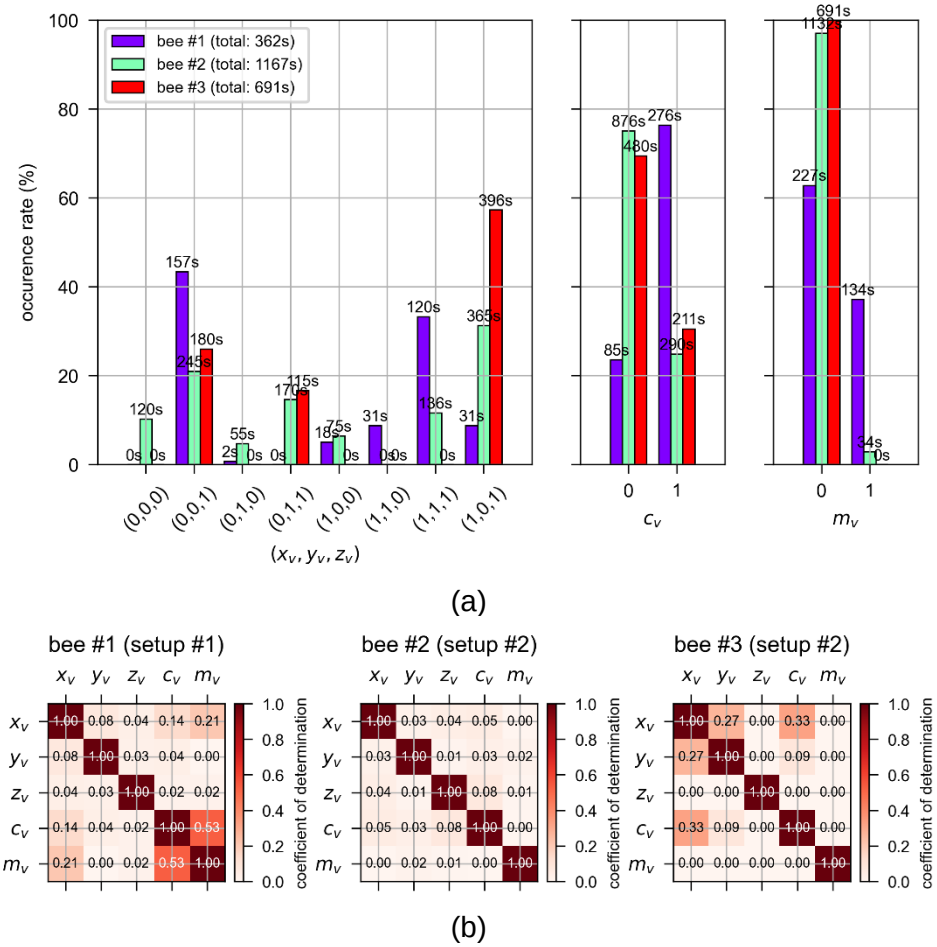

Figure 10 – Statistics of the binary features collected from video recordings: (a) Occurrence rate of the annotated features values for the three tracked bees (bees #1, #2 and #3); (b) Coefficient of determination between all the annotated features for the three tracked bees. See details of annotated features in Table 1.

3.2 Radar analyses

3.2.1 Estimation of the detection volume of the radar detection system

The estimation accuracy of the target location provided by the detection algorithm proposed in section 2.1.4 is defined as the standard deviation of the 3D distribution of estimated locations of stationary targets. The distribution is here obtained from N_m (=500) successive 3D radar scans of the scene in which the stationary target is placed. Two small targets are used separately in the experimental environment shown in Figure 13a: a small 5mm-diameter metallic ball (target #1, see Figure 11b) having a Radar Cross Section (-47dBsm) close to that of a bumblebee (*B. terrestris*), and a 5mm-diameter metallic ball glued to a 2cm-long metallic cylinder (target #2, Figure 11c), which models the radar signature of a bumblebee equipped with a small cylinder tag or antenna placed vertically on its thorax. The estimation accuracy of the detection algorithm is computed from the N_p=30 target locations displayed in Figure 11d.

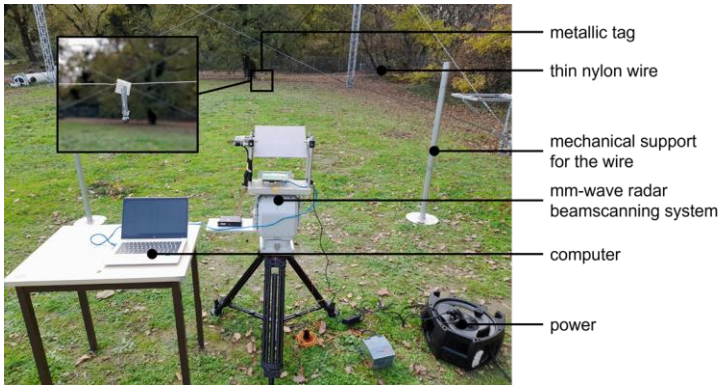

(a)

(b)

(c)

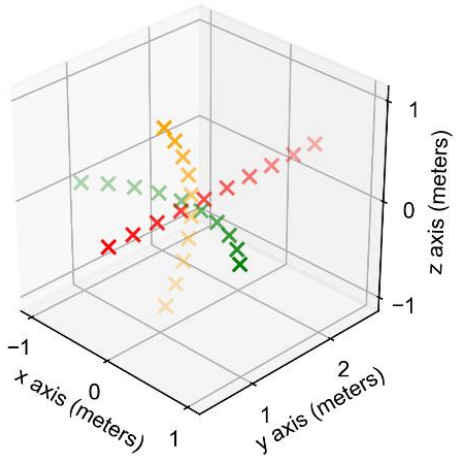

(d)

Figure 11 – (a) photo of the experimental setup to evaluate the estimation accuracy of target location from mm-wave imaging system; (b) photo of the 5mm-diameter metallic ball (target #1), (c) photo of the 5mm-diameter metallic ball glued to a 2cm-long metallic cylinder (target #2), (d) target locations chosen to determine the estimation accuracy of the target location. A total of N_p=30 different target locations were selected: 10 different radar-to-target distances R ranging from 0.4m to R=3.0m with φ=0° and θ=90° (red crosses); 10 azimuth angles φ ranging from -45° to 45° with R=1.4m and θ=90° (green crosses); and 10 elevation angles θ ranging from 50° to 130° with R=1.4m and φ=0° (orange crosses).

The estimated accuracies on the range, elevation and azimuth of targets for N_p tested locations are shown in Figure 11d. The target #2 (metallic ball glued with metallic cylinder) was detected in many more (21/30) tested locations than the target #1 (only metallic ball) (12/30). We defined the detection volume of the detection system as the volume in which the uncertainty on the target location was lower than a predefined threshold. From our tests, we could infer that the detection volume in which the location uncertainty did not exceed 30cm is of 0.19m^3 for the target #1 and of 5.25m^3 for the target #2. The target detection rate (the ratio between the total number of target detections and the total number of observable detections) was found to be on average 78% for target #1 and 67% for target #2. The absence of target detection in some 3D frames may be explained by the fact that the radar beam scanned in elevation is pointed towards the static target at a different elevation angle in each 3D frame (see section 2.1.2). The obtained detection volume of the proposed detection system did not enable the system to track an insect in 3D over large spatial scales (hundreds of meters) but may be used to track an insect in 3D in smaller volumes which is already interesting from an ethological point-of-view to study the insect navigational behavior (see Introduction).

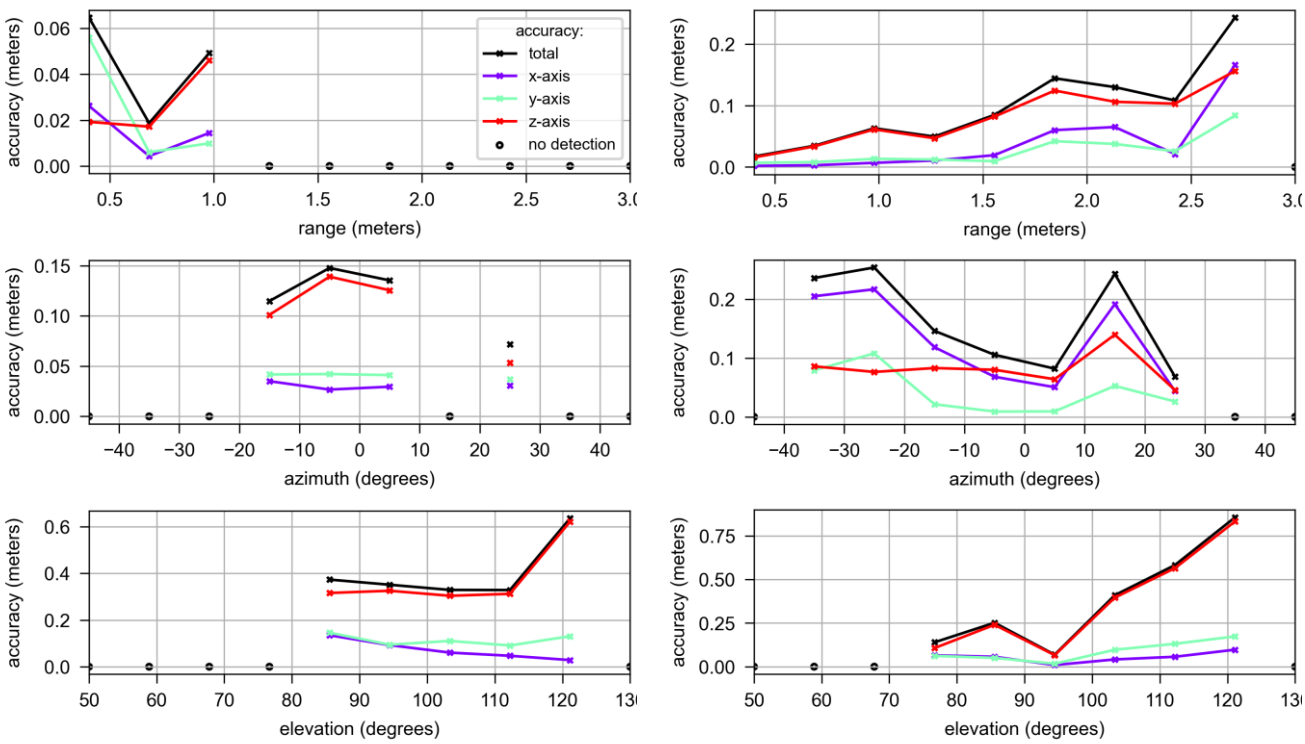

(a) (b)

Figure 12 – Estimation accuracy of the detection system for target locations specified in Figure 11a: for the target #1 (only metallic ball) (a) and for the target #2 (metallic ball glued to metallic cylinder) (b). For each target, the estimated accuracy is given for the $N_{p,R}$ tested range locations (top row), for the $N_{p,\varphi}$ tested azimuth locations (middle row) and for the $N_{p,\theta}$ tested elevation locations (bottom row). The estimated accuracy (total error) is computed for the Euclidean norm of the error along x-axis, the error along y-axis and the error along z-axis. The accuracy estimation for which the detection rate is lower than 10% is indicated as "no detection" in the figures.

3.2.2 3D tracking of bumblebees

3D tracks of bees were extracted from the radar system recordings using the methods described in Section 2 and are displayed in Figure 13. The origin of the spatial representations of estimated flight path is set at the center of the rotating axis of the radar beam-scanning system. In Figure 13a, (x_r, y_r, z_r) denote the estimated Cartesian coordinates of the bee derived from the radar system and v_r denotes the instantaneous speed of the bee estimated from the radar detection system. The polynomial interpolation of 3D motion tracks was reconstructed from the time-domain collection of bee detections shown in Figure 13a. Statistics for the bee coordinates derived from the radar detection algorithm are given in Figure 14. The average estimated speed of detected bees was of 0.33m/s for bee #1, 0.18m/s for bee #2, 0.10m/s for bee #3. These results are consistent with those obtained from video recordings (Figure 10). Moreover, we observed that the distances traveled by bee #1 are smaller than those

426 traveled by bee #2 and bee #3. This is explained by the fact that bee #1 was inside a smaller confinement
427 volume than that of bees #2 and #3. The maximum detection range of bees was of 1.77m.

428 To estimate the quality of the 3D tracks, we defined the bee detection rate as the ratio between the total
429 number of bee detections in our dataset and the total number of observable detections. The total number
430 of observable detections provided by the radar system is the product between the scan rate of the radar
431 system (16.7 scans/s) and the recording time of a given bee. For instance, there were 6,045 observable
432 detections for bee #1. The resulting estimated detection rates were of 10% (617/6,045) for bee #1,
433 18% (3,520/19,489) for bee #2, and 13% (1,464/11,540) for bee #3. These rates were low because
434 they are computed with respect to all observable detections, including those obtained when bees were
435 flying near objects in the environment that are highly reflective to electromagnetic waves. In these
436 situations, the radar echo of bees is completely masked by that of these objects and therefore, bees
437 cannot be detected by the radar system. If we remove such well-known masking situations from
438 observable detections, more realistic detection rates were found. They were found to be of
439 43% (617/1,420) for bee #1, 24% (3,520/14,629) for bee #2, 18% (1,464/8,016) for bee #3. These
440 detection rates are still small compared to the average detection rate (67%) for the static target #2
441 (metallic ball glued with metallic cylinder) used in section 3.2.1. Some missing detections may be
442 attributed to time-dependent electromagnetic clutter (e.g. movement of the cage surfaces during the
443 experiments) that is not possible to mitigate (further discussed in section 4.7) and others may be
444 attributed to the changing orientation of the metallic tag (and thus its changing reflectivity) while the bee
445 is moving inside the cage.

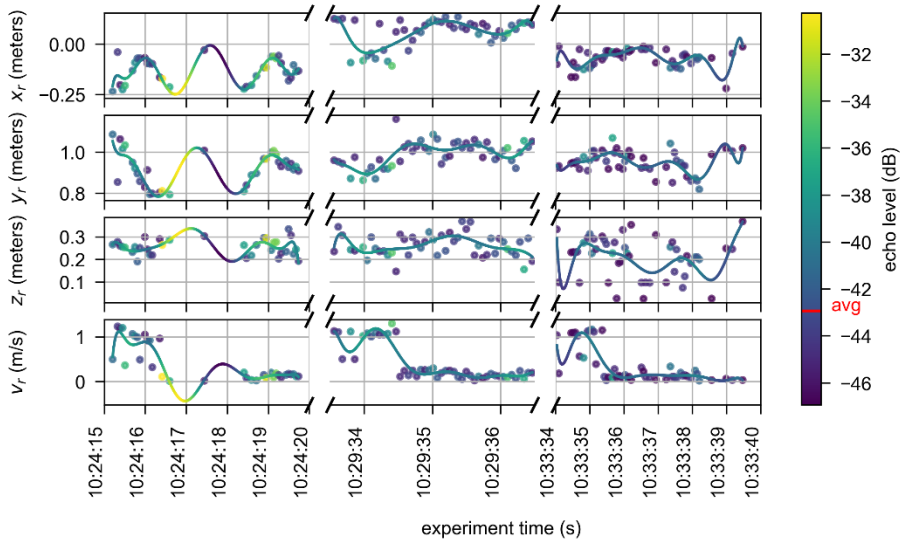

(a)

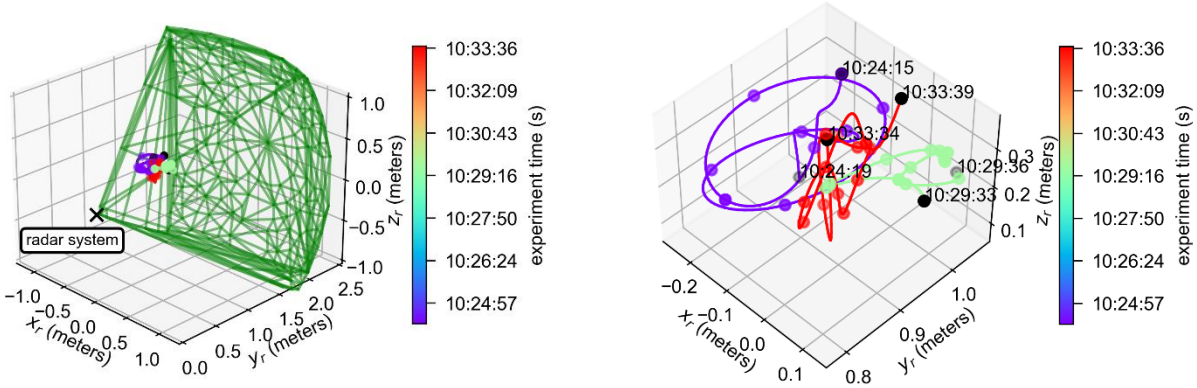

(b) (c)

Figure 13 - 3D motion tracks of a bee (bee #1): (a) Estimated spatial coordinates x_r, y_r, z_r and speed v_r of the bee as a function of time; (b) Representation of the reconstructed 3D flight path (from pink to red). The location of the radar system is shown by the black cross. The radar detection volume (derived from Figure 12) is displayed as a green meshed polygon; (c) Detailed view of the reconstructed 3D flight path.

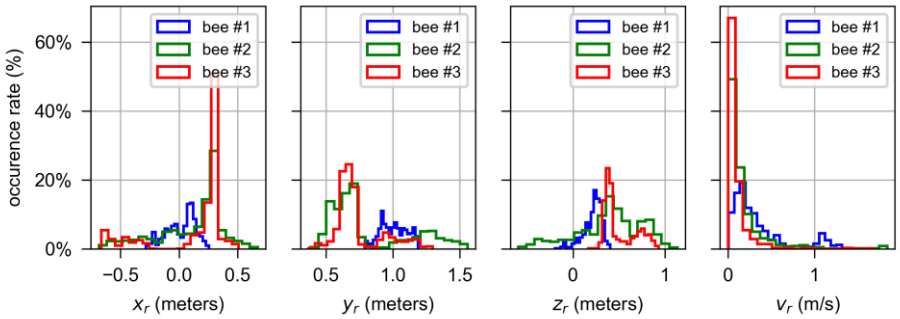

Figure 14 – Statistics of the bee location estimated from the radar detection system: (a) bee #1; (b) bee #2 and (c) bee #3.

3.3 Validation of 3D motion tracks obtained from the radar system

To compare detections obtained from the radar recordings and those extracted from the video recordings, the continuous features (x_r, y_r, z_r, v_r) were transformed in binary categorical features ($x_{r,b}$, $y_{r,b}$, $z_{r,b}$, $m_{r,b}$). The binary classification rules were derived from the ground-truth measurement of the barycenter of the confinement volume given in Table 2. Classification accuracy results are shown in Figure 15. The spatial coordinates of bee #1 have been correctly estimated by the radar system in 90% of the target detections along the x axis and in 64% of the target detections along the y axis. The features $z_{r,b}$ and $m_{r,b}$ have been classified correctly in more than 95% of the occurrences. However, the collected data along the variables z and m was largely imbalanced and thus measuring the classification accuracy did not reflect classification performance of the smaller-sized class (e.g., class z=0 for bee #1). The spatial distribution of the reference clutter contributors for both setups is given in Figure 16. The large occurrence peak observed around x_r=0.0m in the distribution of x_r reflects the electromagnetic clutter generated by the portion of the confinement volume that faced the radar system.

Table 2 - Classification rules for the two experimental setups (#1 and #2) (see Table 1 for features definition).

values	$x_{r,b}$	$y_{r,b}$	$z_{r,b}$	$m_{r,b}$
setup #1 – cellophane box				
0	x_r<0.02m	y_r<0.93m	z_r<-0.10m	v_r<0.10m/s
1	x_r≥0.02m	y_r≥0.93m	z_r≥-0.10m	v_r≥0.10m/s
setup #2 – polyester net				
0	x_r<0.00m	y_r<0.93m	z_r<0.10m	v_r<0.35m/s
1	x_r≥0.00m	y_r≥0.93m	z_r≥0.10m	v_r≥0.35m/s

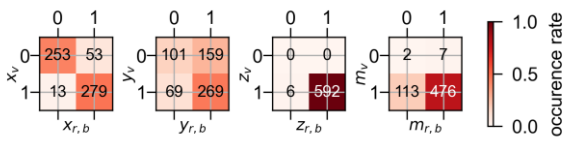

(a)

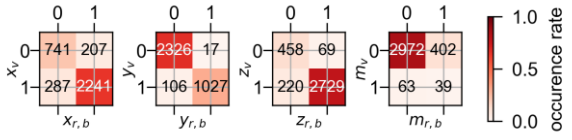

(b)

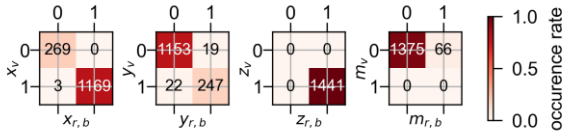

(c)

Figure 15 - Confusion matrices for each recorded feature for: (a) bee #1, (b) bee #2, and (c) bee #3.

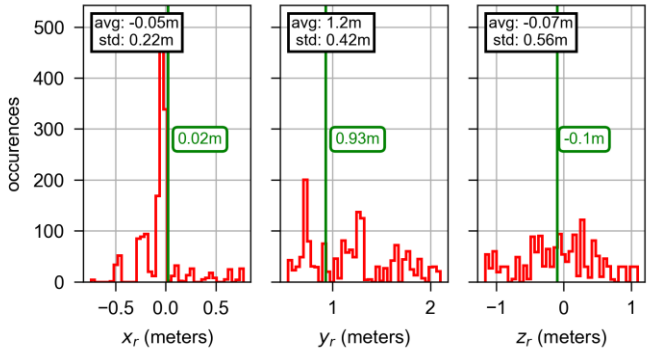

(a)

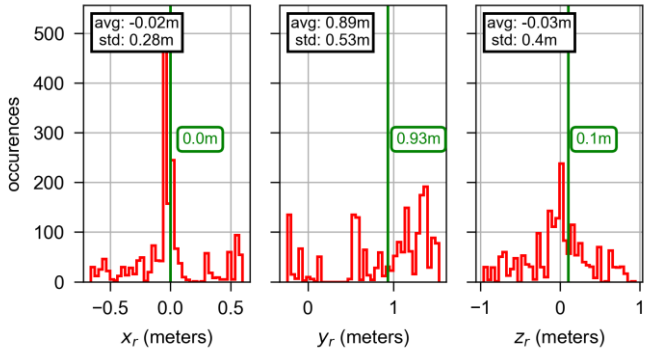

(b)

Figure 16 – Spatial distribution of reference clutter contributors obtained from the clutter mitigation process (step *ii*, section 2.1.4): (a) for setup #1, (b) for setup #2. Statistical distributions along the x, y, and z axes are represented in red and the thresholds for classification are represented in green.

3.4 Using a network of multiple radar systems to increase detection volume

Increasing the detection volume can be performed by using multiple radar imaging systems, each illuminating a different region of the environment. To demonstrate this assertion, we moved a metallic target in front of three radar beam-scanning systems shown in Figure 17. The target was a metallic (aluminium) cylinder of 2cm long and 3mm wide, and was attached to a nylon wire, which in turn was attached to a rod. We moved manually this target in front of the 3 radars along x-axis back-and-forth, while the imaging systems scanned simultaneously the scene. The ground-truth locations of the radar relatively to the chosen origin of the setup were measured (see Table 3) with measurement uncertainties of 1cm for distances and 1° for angles. The total detection volume of the proposed radar beam scanning systems network in which the target used in section 3.3 is detected accurately (that is, with estimated accuracy detailed in Figure 12) is found to be 11.1m^3. We applied the tracking process described in section 2.1.4 for the radar recordings collected by the three imaging systems. We assumed that the three radar beam scanners were synchronously collecting radar data. A unique joint target track was generated by joining the sets of target detections collected by each radar system (#1, #2 and #3) and sorting by increasing timestamp. We observed that the moving target is successfully tracked during the entire duration of the radar recordings (see Figure 18b).

Table 3 - Configuration of the setup using identical 3 radar beam-scanning systems. The coordinate system is defined in Figure 20.

radar	x (m)	y (m)	z (m)
radar #1	-0.75	-0.75	0
radar #2	0	0.75	0
radar #3	0.75	-0.75	0

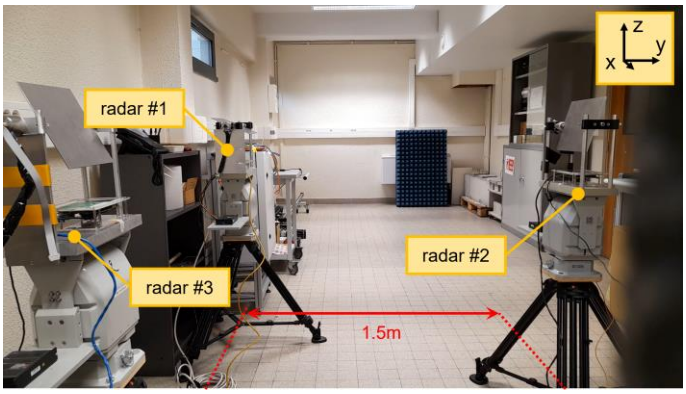

Figure 17 – Photo of set up with three identical radar beam-scanning systems (radar #1, radar #2 and radar #3).

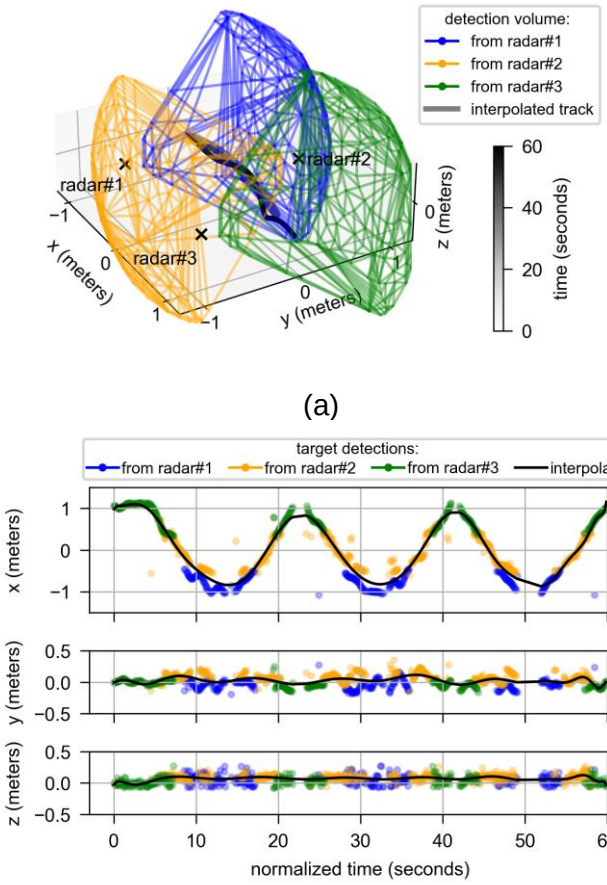

494

495 **Figure 18 – Estimation of the spatial coordinates of a small target (metallic cylinder of 2cm long and 3mm wide) moving**
496 **back-and-forth along x-axis from 3 radar imaging systems: (a) representation of the 3 detection volumes brought by**
497 **each radar system (the joint detection volume is of 3.2m^3); (b) estimated spatial coordinates x, y, z of the target as a**
498 **function of time (detections of radar #1 are in blue, of radar #2 are in orange, and of radar #3 are in in green and the**
499 **estimated spatial coordinates of the associated polynomial interpolation is shown in black).**

500 # 4 Discussion

501 We demonstrated that mm-wave radar technology can be used to track the motion of individual flying
502 insects with high resolution. A single mm-wave FM-CW radar sensor can be used for such tracking in a
503 detection volume of 5.3m^3 (up to a radar-to-target distance of 2.6m). From ground-truth video validation,
504 3D tracks obtained from the radar sensor were correct in 82% of the time. Our approach is thus robust
505 and holds many promises for future behavioral research on flying insects in the field as it is low cost,
506 transportable, insensitive to light conditions, requires one sensor for resolving 3D, can track through
507 certain electromagnetic clutter, may eventually track several insects simultaneously, and can be

duplicated and combined to increase tracking volumes. Tracking with mm-wave radars is therefore potentially applicable to a wide range of animals and at different spatial scales.

4.1 Performance comparison with state-of-the-art technologies used to track flying insects

Our new radar-based tracking system fills an important gap for future research on insect behavior. An overview of a state of the art in flying insect tracking technology is given in Table 4. The mm-wave solution proposed here allows to track an insect in 3D in a larger volume than optical technologies. At these spatial scales, harmonic radars and radiotelemetry can only track in 2D (Kennedy et al., 2018; Riley et al., 1996). In a previous work, we demonstrated that radar detection of an insect is possible without a tag (Dore et al., 2020). Here we showed that appending a metallic tag (here a metallic cylinder) to the same target increased the detection volume of the radar from $3.6m^3$ to $5.3m^3$. We also showed that the detection volume of the radar system can be considerably increased by combining several radar units thereby opening the possibility to work at much larger spatial scales. Finally, although we have illustrated the utility of our system for tracking bumblebees, in principle mm-wave radars can track virtually any kind of small (flying or not) animals provided it can carry a passive metallic tag. Tracking and posture monitoring of larger untagged animals using a similar approach was previously demonstrated (Dore et al., 2021; Henry et al., 2023).

Table 4 – State of the art of insect tracking technology. If not explicitly mentioned in the paper, the feature value was estimated from other data in the paper. N/A means Not Applicable.

technology	dimension of the detection domain	detection range, surface or volume	spatial resolution (meter)	time resolution (frame per sec)	real-time image processing	goal	number of separate sensors	passive or active tag	tag weight (mg)	reference
HF RFID	1D	2.4mm	N/A	10	no	detection and id	1	passive	5	(Ohashi et al., 2010)
visible optics	1D	0.1m	N/A	60	no	detection	1	no tag	N/A	(Lihoreau et al., 2016a)
harmonic radar	2D	800m	2	3	no	tracking	1	passive	15	(Woodgate et al., 2017)
harmonic radar	2D	250m	7	20	no	tracking	1	passive	3	(Riley et al., 1996)
radio-telemetry	2D	800m	10	1	no	tracking	1	active	280	(Kennedy et al., 2018)
harmonic radar	2D	900m	10	1	no	tracking	1	passive	12	(Tahir and Brooker, 2011)
IR optics	2D	$0.03m^2$	0.001	2	yes	id	2	passive	2.4	(Crall et al., 2018)
IR optics	2D	$0.05m^2$	0.001	20	no	detection and id	2	no tag	N/A	(Manoukis and Collier, 2019)
visible optics	2D	$0.03m^2$	0.001	1	yes	id and tracking	1	passive	1.8	(Crall et al., 2015)
visible optics	2D	$0.2m^2$	0.001	60	no	id and tracking	1	no tag	N/A	(Ratnayake et al., 2021)
IR optics	2D	$2.0m^2$	0.1	100	yes	tracking	1	passive	13	(Walter et al., 2021)
UHF RFID	3D	$1.0m^3$	0.1	100	no	id and tracking	4	passive	3	(Särkkä et al., 2014)
visible optics	3D	$0.5m^3$	0.01	50	yes	id and tracking	3	no tag	N/A	(Lihoreau et al., 2016b)
visible optics	3D	$27m^3$	0.1	60	no	tracking	2	no tag	N/A	(Sun and Gaydecki, 2021)
stereo optics	3D	$0.06m^3$	0.1	47	no	tracking	1	no tag	N/A	(Chiron et al., 2013)
stereo optics	3D	N/A	N/A	160	N/A	detection	1	passive	20	(Vo-Doan et al., 2023)
depth IR optics	3D	$0.8m^3$	0.1	30	no	tracking	1	no tag	N/A	(Nasir et al., 2023)
visible optics	3D	$0.01m^3$	0.01	60	no	tracking and posture	3	no tag	N/A	(Ahmed and Faruque, 2022)
visible optics	3D	$0.001m^3$	0.001	20	no	tracking and posture	1	no tag	N/A	(Chen et al., 2021)
mm-wave radar	3D	$3.6m^3$	0.05	16.7	no	tracking	1	no tag	N/A	(Dore et al., 2020)
mm-wave radar imaging system	**3D**	**$5.3m^3$**	**0.05** *	**16.7**	**no**	**tracking**	**1**	**passive**	**50**	**this work**

* resolution in elevation is 6° and theoretical resolution is azimuth is 0.35°

4.2 About the detection rate

Our proposed detection algorithm enabled to extract target detections from images obtained from the radar sensor. The overall target detection rate was found to be τ_d=15% (5,601/38,428). This implies

that on average, from one in every seven radar scanning samples, a target detection could be derived. Thus, the average target detection sampling rate was $\tau_d f_{scan}$=2.5detections/s. In our experiments, the bumblebees moved in the constrained volume at an average speed of 0.18m/s, thus an individual moving at this average speed would be detected on average every 0.07m. In an unconstrained space, a flying bee typically moves at an average speed of 4m/s which means that the detection spatial resolution would be as high as 1.6m using the average target detection sampling rate obtained from our experiments. However, this detection spatial resolution does not account for the varying posture of the tagged individuals (and thus the tag orientation) relatively to the radar system during the radar scanning, and the inevitable time-dependent electromagnetic clutter (see section 4.7).

4.3 About the post-processing runtime

The averaged processing time (computed over 15,000 samples) to generate one 3D image from raw radar data applying the 2D-MUSIC algorithm was of about 13.2 seconds per 3D image. This implies that the runtime to process a 30 seconds long radar recording was in average 500×13.2s=110min. This computation was performed on a HPC (High-Performance Computing) cluster of 16 CPUs (Intel E5-2695 v4 2.1G) mounted in parallel using a total random-access memory (RAM) of 240GB. The resulting 3D-frame file has a size on disk on average of about 2.32MB. This implies that the size on disk of a 30 seconds long radar recording is on average 500×2.32MB=1.16GB. Although real-time image processing is not currently yet achievable with this tracking system, processing time and used disk space can be reduced by decreasing the padding factor at the cost of less resolution in the final 3D images. Another solution to reduce data size would be to crop radar images using spatial bounds enclosing a smaller volume in which the target did not exit during the radar scanning. To justify the use of a 2D-MUSIC algorithm to our application, we compared the detection accuracy performance resulting from the analysis of images obtained by applying the implemented 2D-MUSIC algorithm raw data and that resulting from the analysis of images obtained by applying the 2D-beamformer algorithm on the raw data. To illustrate this comparison, we used the radar data collected from the radar measurements

performed to characterize the detection systems' detection volume in section 3.3. From the estimated accuracy results shown in the Figure S3 in the Supplementary data section, we can infer that the detection volume of the detection system using the 2D-beamformer algorithm (0.57m^3) is significantly lower than that of the detection system using the 2D-MUSIC algorithm (5.25m^3). Thus, although the 2D-beamformer algorithm is faster (0.9 seconds per 3D image) than the 2D-MUSIC algorithm (13.2 seconds per 3D image), the 2D-MUSIC algorithm provides a better detection performance than the 2D-beamformer algorithm. Other discrete source DOA estimation algorithms will be tested in future studies to improve the efficiency of the detection process and reduce the computation time.

4.4 About potential improvements on the flying insect tracking system

The proposed tracking system presents encouraging results. Using metallic tags allowed to track a tagged flying insect within bounds of a confinement box. This flight constraint allowed to collect significantly more and longer 3D tracks than those obtained of untagged insects in previous work (Dore et al., 2020) while requiring significantly less overall experiment time (i.e. only a few minutes). The detection rate has been estimated to evaluate the quality of the obtained tracks. Information obtained manually from ground-truth video recordings have allowed to confirm the 3D tracks obtained by the radar 3D beam-scanning system.

While our 3D tracking radar system allows filling an existing technological gap, more improvements can be made to meet the needs of biologists and ecologists for tracking flying individuals in 3D with high resolution and in a large volume. Temporal resolution of the imaging system may be improved by increasing measurement rate of the radar sensor. Detection rate and volume may also be improved by increasing transmitted power or radar sensitivity. Although, per the radar link equation, doubling the radar-to-target distance while keeping a fixed radar sensitivity requires to multiply the transmitted power by 2^4=16. In a more practical sense, as the radar sensor used in our experiments features a maximum transmitted power of 10mW, the transmitted power that would be needed to detect a target at twice the

actual maximum distance of detection is 160mW. Managing signals carrying such power would require more costly hardware. A much cheaper solution to increasing detection volume is to utilize a network of multiple identical tracking FM-CW radar systems, as we have demonstrated in section 3.4.

As mentioned in the introduction, mounting imaging systems on UAVs to track insects on large spatial scales has been investigated (Ju and Son, 2022; Kim et al., 2022; Lavrenko et al., 2021; Vo-Doan et al., 2023). Embarking our radar imaging system on a UAV would require integrating a computer on the UAV and reducing the mass of the overall imaging system. A more light-weight imaging system can be achieved from choosing a lighter-weight rotating reflector (e.g. a metallic mesh grid) thus reducing the motor torque needed to rotate the reflector at currently used angular speed. Thus a smaller less power-consuming motor could be used instead of the one currently used to make the reflector rotate. The mm-wave radar sensor itself is already light-weight compared to the mass of the mechanical beam-scanning system. The effect of the air flow during flight on this beam-scanning system mounted on an UAV would have to be studied.

4.5 About the detection and the tracking algorithms

In the detection step, local maxima could have been simply detected by a gradient method or another standard peak detection algorithm. However, the proposed segmentation method could be helpful (not shown here) to define specific surfaces or volumes where targets should not be detected. As the future aim of our study is to demonstrate the 3D tracking of flying insects using mm-wave radar as a proof-of-concept, we assumed the presence of a single target and thus no ambiguous track assignments to resolve (see section 2.1.4). However, future field studies require the possibility for the simultaneous tracking of multiple flying insects moving and interacting in the scene, using a multi-target tracking algorithm to solve the induced track assignment problem. In the era of extensive real-time video surveillance, many *Multi-Object Tracking* (MOT) algorithms have been proposed to resolve multiple tracks from a set of detections extracted from sensors in various contexts (Rakai et al., 2022; Smith et

al., 2019). Such an algorithm could be tested for the tracking of multiple bees flying in the same cage using FM-CW radars.

4.6 About deriving target speed from a Doppler analysis

As mentioned in section 2.1.2, estimating the velocity directly from the radar data by applying a Doppler analysis is not possible using the current 3D beamscanning system because the radar beam is steered in elevation which would invalidate a Doppler analysis. As a potential solution, the use of three mm-wave FM-CW radars working in range-Doppler mode would allow estimating the 3D location of a target within the intersection volume of the three radar beams. Each radar would be oriented along one axis of the Cartesian coordinates in order to estimate the 3D location of a target (see Figure 19). The 3D location would be resolved from the range and velocity detection from each radar system. Using the 77GHz FM-CW radar commercialized by INRAS, the radar beam generated by this radar has a half-power beamwidth in E-plane of 13.2° and a half-power beamwidth in H-plane of 51°. So far the volume of the radar beam generated by a single radar sensor is of 6.7m^3 for a maximum range of 5meters. Therefore, even assuming that the target would be detectable up until 5 meters, the intersection region of the three radar beams in which a target would be detectable would have a volume of only 1.79m^3 which is smaller than the detection volume obtained by the 3D beamscanner system. Thus, the specific radar sensor used in this study would not a good choice for multistatic range-Doppler 3D location estimation. A radar sensor generating a larger radar beam would be a better fit for this purpose.

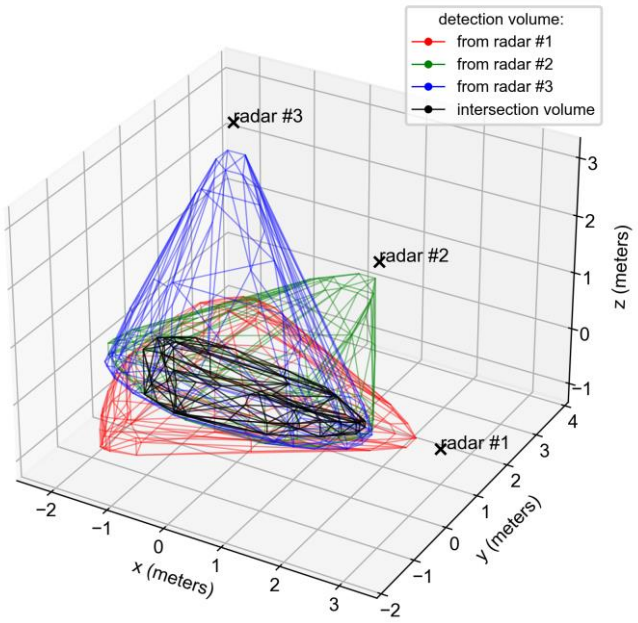

Figure 19 - 3D representation of the radar beams generated by the three mm-wave radar sensors, each oriented towards one axis of the Cartesian coordinates (x, y, z).

4.7 About electromagnetic clutter

The calibration step of the radar setup is necessary to mitigate the electromagnetic clutter generated by the bounds of the confinement volume. The so-called 3D-space reference image obtained from this calibration allows to mitigate static electromagnetic clutter. However, in the carried-out outdoors experiments, bounds of the confinement volume were slightly moving due to wind thus generating time-varying electromagnetic clutter. These variable undesirable radar echoes, which may generate false detections, cannot be mitigated by the above-described calibration technique. Setting spatial limits to select detections in the volume of interest allowed the mitigation of this time-varying electromagnetic clutter.

4.8 About the passive tag attached to the insect

Finally, the tag's mass (13% of an average bumblebee's weight) is large compared to the mass of harmonic radar tags (5%) but low compared to the mass of radio-telemetry active tags (75%). Future

637 improvements of tag design may come up with lighter tags. Importantly, the simple design of our passive
638 tags also opens the door for creating tags with different electromagnetic signatures for tracking multiple
639 individually identified insects flying simultaneously in the scanned scene, which is currently impossible
640 with harmonic radar systems. Multi-target tracking is readily possible with mm-wave radars as we have
641 demonstrated before (Dore et al., 2021, 2020). Moreover, in future work, we aim to study the impact of
642 the tag weight on the insect movement and flight.

643 ## 4.9 About the implementation of tracking in the case of a network of several
644 radar systems

645 In section 3.4, we demonstrated the tracking of a tag for a network of three radar beamscanners. To
646 ensure the detection set obtained from each radar beamscanner had the same spatial reference, we
647 measured the location and orientation of each radar beamscanner relatively to an origin. However, there
648 may be a small timestamp delay between one radar beamscanner and another radar beamscanner.
649 Indeed, as the speed of each separate motor varies along time, (as mentioned in section 2.1.2), it is not
650 possible to synchronize the three mechanical beamscanners to point at the same time at the same
651 elevation angle. Therefore, the maximum timestamp difference between the timestamp recorded when
652 radar #1 points in a given elevation angle and that recorded when radar points at the same elevation
653 angle is of 60ms, i.e. the duration required for a 360° elevation beam scanning. Moreover, we assume
654 that tracks collected by the three radar systems are those of the target of interest. All the detections of
655 the three tracks (one per radar system) are then added in a single set that gives the total track of a
656 single target. The spatial interpolation (over time) of the total track is shown on figure 19b.

657 # 5 Conclusions

658 Our method based on a mm-wave radar imaging system for tracking passively tagged flying insects in
659 3D provides promising results. For verification purposes, tracks collected by the radar system have been
660 compared to those extracted from video recordings. From this comparison, correctly identified 3D tracks
661 of tagged flying individuals collected by the radar system add up to a total of 5.2 minutes. Potential

improvements on the radar system are proposed to increase its detection volume of tagged flying individuals and track multiple identified individuals simultaneously, thereby providing new experimental opportunities for research in insect behaviour and ecology.

CRediT authorship contribution statement

Etienne Dedic: Conceptualization (radar detection, experimental protocol), Investigation (measurements, video annotations, signal processing), Data Curation, Writing – original draft, Writing – review & editing. **Dominique Henry:** Conceptualization (radar detection), Writing – review & editing. **Mathieu Lihoreau:** Resources (electrical and hive management), Writing – review & editing, Funding acquisition. **Hervé Aubert:** Conceptualization (radar detection), Supervision, Writing – review & editing, Funding acquisition.

Declaration of competing interest

The authors declare that they have no known competing financial interests or personal relationships that could have appeared to influence the work reported in this paper.

Data availability

Data will be made available on request.

Acknowledgements

We thank the ANR (French Research Agency) and the DDG (German Research Foundation) for financial support through the 3DNaviBee project (ANR-19-CE37-0024). We thank the ERC (European Research Council) for financial support through the Bee-Move project (GA101002644).

References

Ahmed, I., Faruque, I.A., 2022. High speed visual insect swarm tracker (Hi-VISTA) used to identify the effects of confinement on individual insect flight. Bioinspir. Biomim. 17, 046012. https://doi.org/10.1088/1748-3190/ac6849

Batsleer, F., Bonte, D., Dekeukeleire, D., Goossens, S., Poelmans, W., Van der Cruyssen, E., Maes, D., Vandegehuchte, M.L., 2020. The neglected impact of tracking devices on terrestrial arthropods. Methods Ecol. Evol. 11, 350–361. https://doi.org/10.1111/2041-210X.13356

Chen, C.-H., Chiang, A.-S., Tsai, H.-Y., 2021. Three-Dimensional Tracking of Multiple Small Insects by a Single Camera. J. Insect Sci. 21, 14. https://doi.org/10.1093/jisesa/ieab079

Chiron, G., Gomez-Krämer, P., Ménard, M., 2013. Detecting and tracking honeybees in 3D at the beehive entrance using stereo vision. EURASIP J. Image Video Process. 2013, 59. https://doi.org/10.1186/1687-5281-2013-59

Chittka, L., 2022. The mind of a bee. Princeton University Press, Princeton.

Crall, J.D., Gravish, N., Mountcastle, A.M., Combes, S.A., 2015. BEEtag: A Low-Cost, Image-Based Tracking System for the Study of Animal Behavior and Locomotion. PLOS ONE 10, e0136487. https://doi.org/10.1371/journal.pone.0136487

Crall, J.D., Switzer, C.M., Oppenheimer, R.L., Ford Versypt, A.N., Dey, B., Brown, A., Eyster, M., Guérin, C., Pierce, N.E., Combes, S.A., de Bivort, B.L., 2018. Neonicotinoid exposure disrupts bumblebee nest behavior, social networks, and thermoregulation. Science 362, 683–686. https://doi.org/10.1126/science.aat1598

Dedic, E., Hadj Djilani, A., Henry, D., Lihoreau, M., Aubert, H., 2023. 3D Tracking of Small Moving Targets in Cluttered Environment from the Isolines Processing of Millimeter-wave Radar Images, in: 2023 IEEE International Symposium on Antennas and Propagation and USNC-URSI Radio Science Meeting. Presented at the IEEE APS-URSI 2023, IEEE Xplore, Portland, Oregon, USA. https://doi.org/10.1109/USNC-URSI52151.2023.10237829

Dore, A., Henry, D., Lihoreau, M., Aubert, H., 2020. 3D Trajectories of Multiple Untagged Flying Insects from Millimetre-wave Beamscanning Radar, in: 2020 IEEE International Symposium on Antennas and Propagation and North American Radio Science Meeting. Presented at the 2020 IEEE International Symposium on Antennas and Propagation and North American Radio Science Meeting, pp. 1209–1210. https://doi.org/10.1109/IEEECONF35879.2020.9329732

Dore, A., Pasquaretta, C., Henry, D., Ricard, E., Bompard, J.-F., Bonneau, M., Boissy, A., Hazard, D., Aubert, H., Mathieu, L., 2021. A non-invasive radar system for automated behavioural tracking: application to sheep. https://doi.org/10.1101/2020.12.09.418038

Drake, V.A., Reynolds, D.R., 2013. Radar Entomology: Observing Insect Flight and Migration. Anim. Behav. 86, 659–660. https://doi.org/10.1016/j.anbehav.2013.05.035

Finn, H., Johnson, R., 1968. Adaptive detection mode with threshold control as a function of spatially sampled clutter level estimates. RCA Rev. 43, 414–464.

Freeman, R.B., 1968. Charles Darwin on the routes of Male Humble Bees. Bull. Nat. Hist. Mus. Nat. Hist. Hist. Ser. 3, 177–189. https://doi.org/10.5962/p.314502

Henry, D., Aubert, H., 2019. Isolines in 3D Radar Images for Remote Sensing Applications. Presented at the 2019 16th European Radar Conference (EuRAD).

Henry, D., Bailly, J., Pasquereau, T., Bompa, J.-F., Aubert, H., Canario, L., 2023. Monitoring of sow postural activity from 3D millimeter-wave radar imaging. Comput. Electron. Agric. 213, 108214. https://doi.org/10.1016/j.compag.2023.108214

Ings, T.C., Chittka, L., 2008. Speed-Accuracy Tradeoffs and False Alarms in Bee Responses to Cryptic Predators. Curr. Biol. 18, 1520–1524. https://doi.org/10.1016/j.cub.2008.07.074

INRAS, 2023. RadarBooK2 INRAS [WWW Document]. URL https://inras.at/en/radarbook2/ (accessed 12.1.23).

Ju, C., Son, H.I., 2022. Investigation of an Autonomous Tracking System for Localization of Radio-Tagged Flying Insects. IEEE Access 10, 4048–4062. https://doi.org/10.1109/ACCESS.2022.3140488

Kaláb, O., Musiolek, D., Rusnok, P., Hurtik, P., Tomis, M., Kočárek, P., 2021. Estimating the effect of tracking tag weight on insect movement using video analysis: A case study with a flightless orthopteran. PLOS ONE 16, e0255117. https://doi.org/10.1371/journal.pone.0255117

Kays, R., Crofoot, M.C., Jetz, W., Wikelski, M., 2015. Terrestrial animal tracking as an eye on life and planet. Science 348, aaa2478. https://doi.org/10.1126/science.aaa2478

Kennedy, P.J., Ford, S.M., Poidatz, J., Thiéry, D., Osborne, J.L., 2018. Searching for nests of the invasive Asian hornet (Vespa velutina) using radio-telemetry. Commun. Biol. 1, 1–8. https://doi.org/10.1038/s42003-018-0092-9

Kim, B., Ju, C., Son, H., 2022. Field evaluation of UAV-based tracking method for localization of small insects. Entomol. Res. 52. https://doi.org/10.1111/1748-5967.12573

Kim, S., Ju, C., Kim, J., Son, H.I., 2019. A Tracking Method for the Invasive Asian Hornet: A Brief Review and Experiments. IEEE Access 7, 176998–177008. https://doi.org/10.1109/ACCESS.2019.2958153

Kissling, W.D., Pattemore, D.E., Hagen, M., 2014. Challenges and prospects in the telemetry of insects. Biol. Rev. Camb. Philos. Soc. 89, 511–530. https://doi.org/10.1111/brv.12065

Lavrenko, A., Barry, Z., Norman, R., Frazer, C., Ma, Y., Woodward, G., Pawson, S., 2021. Autonomous Swarm of UAVs for Tracking of Flying Insects with Harmonic Radar, in: 2021 IEEE 93rd Vehicular Technology Conference (VTC2021-Spring). Presented at the 2021 IEEE 93rd Vehicular Technology Conference (VTC2021-Spring), pp. 1–5. https://doi.org/10.1109/VTC2021-Spring51267.2021.9449074

Lihoreau, M., Chittka, L., Raine, N.E., 2016a. Monitoring Flower Visitation Networks and Interactions between Pairs of Bumble Bees in a Large Outdoor Flight Cage. PLOS ONE 11, e0150844. https://doi.org/10.1371/journal.pone.0150844

Lihoreau, M., Ings, T.C., Chittka, L., Reynolds, A.M., 2016b. Signatures of a globally optimal searching strategy in the three-dimensional foraging flights of bumblebees. Sci. Rep. 6, 30401. https://doi.org/10.1038/srep30401

Manokhin, G.O., Erdyneev, Z.T., Geltser, A.A., Monastyrev, E.A., 2015. MUSIC-based algorithm for range-azimuth FMCW radar data processing without estimating number of targets, in: 2015 IEEE 15th Mediterranean Microwave Symposium (MMS). Presented at the 2015 IEEE 15th Mediterranean Microwave Symposium (MMS), pp. 1–4. https://doi.org/10.1109/MMS.2015.7375471

Manoukis, N.C., Collier, T.C., 2019. Computer Vision to Enhance Behavioral Research on Insects. Ann. Entomol. Soc. Am. 112, 227–235. https://doi.org/10.1093/aesa/say062

Margerie, E. de, Monmasson, K., 2024. Recording butterfly movements from a UAV. https://doi.org/10.1101/2024.07.17.603869

Nasir, A., Ullah, M.O., Yousaf, M.H., 2023. AI in apiculture: A novel framework for recognition of invasive insects under unconstrained flying conditions for smart beehives. Eng. Appl. Artif. Intell. 119, 105784. https://doi.org/10.1016/j.engappai.2022.105784

Ohashi, K., D'Souza, D., Thomson, J.D., 2010. An automated system for tracking and identifying individual nectar foragers at multiple feeders. Behav. Ecol. Sociobiol. 64, 891–897.

Psychoudakis, D., Moulder, W., Chen, C.-C., Zhu, H., Volakis, J.L., 2008. A Portable Low-Power Harmonic Radar System and Conformal Tag for Insect Tracking. IEEE Antennas Wirel. Propag. Lett. 7, 444–447. https://doi.org/10.1109/LAWP.2008.2004512

Rakai, L., Song, H., Sun, S., Zhang, W., Yang, Y., 2022. Data association in multiple object tracking: A survey of recent techniques. Expert Syst. Appl. 192, 116300. https://doi.org/10.1016/j.eswa.2021.116300

Ratnayake, M.N., Dyer, A.G., Dorin, A., 2021. Tracking individual honeybees among wildflower clusters with computer vision-facilitated pollinator monitoring. PLOS ONE 16, e0239504. https://doi.org/10.1371/journal.pone.0239504

Reynolds, D.R., Riley, J.R., 2002. Remote-sensing, telemetric and computer-based technologies for investigating insect movement: a survey of existing and potential techniques. Comput. Electron. Agric. 35, 271–307. https://doi.org/10.1016/S0168-1699(02)00023-6

Rhodes, M.W., Bennie, J.J., Spalding, A., ffrench-Constant, R.H., Maclean, I.M.D., 2022. Recent advances in the remote sensing of insects. Biol. Rev. 97, 343–360. https://doi.org/10.1111/brv.12802

Riley, J.R., Smith, A.D., Reynolds, D.R., Edwards, A.S., Osborne, J.L., Williams, I.H., Carreck, N.L., Poppy, G.M., 1996. Tracking bees with harmonic radar. Nature 379, 29–30. https://doi.org/10.1038/379029b0

Růžičková, J., Elek, Z., 2023. Beetles on the move: Not-just-a-technical review of beetles' radio-tracking. Entomol. Exp. Appl. 171, 82–93. https://doi.org/10.1111/eea.13260

Särkkä, S., Viikari, V., Jaakkola, K., 2014. RFID-based butterfly location sensing system, in: 2014 22nd European Signal Processing Conference (EUSIPCO). Presented at the 2014 22nd European Signal Processing Conference (EUSIPCO), pp. 2045–2049.

Smith, J., Particke, F., Hiller, M., Thielecke, J., 2019. Systematic Analysis of the PMBM, PHD, JPDA and GNN Multi-Target Tracking Filters, in: 2019 22th International Conference on Information Fusion (FUSION). Presented at the 2019 22th International Conference on Information Fusion (FUSION), pp. 1–8. https://doi.org/10.23919/FUSION43075.2019.9011349

Sun, C., Gaydecki, P., 2021. A Visual Tracking System for Honey Bee (Hymenoptera: Apidae) 3D Flight Trajectory Reconstruction and Analysis. J. Insect Sci. 21, 17. https://doi.org/10.1093/jisesa/ieab023

Tahir, N., Brooker, G., 2015. Toward the Development of Millimeter Wave Harmonic Sensors for Tracking Small Insects. IEEE Sens. J. 15, 5669–5676. https://doi.org/10.1109/JSEN.2015.2445933

Tahir, N., Brooker, G., 2011. Recent developments and recommendations for improving harmonic radar tracking systems, in: Proceedings of the 5th European Conference on Antennas and Propagation (EUCAP). Presented at the Proceedings of the 5th European Conference on Antennas and Propagation (EUCAP), pp. 1531–1535.

van Klink, R., August, T., Bas, Y., Bodesheim, P., Bonn, A., Fossøy, F., Høye, T.T., Jongejans, E., Menz, M.H.M., Miraldo, A., Roslin, T., Roy, H.E., Ruczyński, I., Schigel, D., Schäffler, L., Sheard, J.K., Svenningsen, C., Tschan, G.F., Wäldchen, J., Zizka, V.M.A., Åström, J., Bowler, D.E., 2022. Emerging technologies revolutionise insect ecology and monitoring. Trends Ecol. Evol. 37, 872–885. https://doi.org/10.1016/j.tree.2022.06.001

Vo-Doan, T.T., Titov, V.V., Harrap, M.J.M., Lochner, S., Straw, A.D., 2023. High Resolution Outdoor Videography of Insects Using Fast Lock-On Tracking. https://doi.org/10.1101/2023.12.20.572558

Walter, T., Degen, J., Pfeiffer, K., Stöckl, A., Montenegro, S., Degen, T., 2021. A new innovative real-time tracking method for flying insects applicable under natural conditions. BMC Zool. 6, 35. https://doi.org/10.1186/s40850-021-00097-3

Wei, Z., Li, B., Feng, T., Tao, Y., Zhao, C., 2023. Area-Based CFAR Target Detection for Automotive Millimeter-Wave Radar. IEEE Trans. Veh. Technol. 72, 2891–2906. https://doi.org/10.1109/TVT.2022.3216013

Woodgate, J.L., Makinson, J.C., Lim, K.S., Reynolds, A.M., Chittka, L., 2017. Continuous Radar Tracking Illustrates the Development of Multi-destination Routes of Bumblebees. Sci. Rep. 7, 17323. https://doi.org/10.1038/s41598-017-17553-1